

## Quantum synchronization of a single trapped-ion qubit


Liyun Zhang,<sup>1,2,3,\*</sup> Zhao Wang<sup>1,2,3,\*</sup>, Yucheng Wang,<sup>1,2,3</sup> Junhua Zhang,<sup>1,2,3</sup> Zhigang Wu<sup>1,2,3</sup>,  
Jianwen Jie<sup>4,1,2,3,†</sup> and Yao Lu<sup>1,2,3,‡</sup>

<sup>1</sup>Shenzhen Institute for Quantum Science and Engineering (SIQSE), Southern University of Science and Technology, Shenzhen 518055, People's Republic of China

<sup>2</sup>International Quantum Academy, Shenzhen 518048, China

<sup>3</sup>Guangdong Provincial Key Laboratory of Quantum Science and Engineering, Southern University of Science and Technology, Shenzhen 518055, People's Republic of China

<sup>4</sup>Shenzhen Key Laboratory of Ultraintense Laser and Advanced Material Technology, Center for Advanced Material Diagnostic Technology, and College of Engineering Physics, Shenzhen Technology University, Shenzhen 518118, China

 (Received 17 May 2022; revised 29 August 2023; accepted 12 September 2023; published 25 September 2023)

Synchronizing a few-level quantum system is of fundamental importance to the understanding of synchronization in the deep quantum regime. Whether a two-level system, the smallest quantum system, can be synchronized has been theoretically debated for the past several years. Here, for the first time, we demonstrate that a qubit can indeed be synchronized to an external driving signal by using a trapped-ion system. By engineering fully controllable gain and damping processes, an ion qubit is locked to the driving signal and oscillates in phase. Moreover, upon tuning the parameters of the driving signal, we observe characteristic features of the Arnold tongue as well. Our measurements agree remarkably well with numerical simulations based on recent theory on qubit synchronization. By synchronizing the basic unit of quantum information, our study opens up the possibility of exploring the application of quantum synchronization to quantum information processing in the near future.

DOI: [10.1103/PhysRevResearch.5.033209](https://doi.org/10.1103/PhysRevResearch.5.033209)

### I. INTRODUCTION

Originally discovered by Huygens in two pendulum clocks suspended from the same wooden beam [1], synchronization is widespread in nature [2–7]. Systems capable of synchronization usually suffer from certain dissipations, holding a common characteristic known as the *limit cycle*. It represents the steady motion of the system at the intrinsic oscillating frequency, possessing one or more free phases and being robust to perturbations. Owning a limit cycle enables a self-sustained oscillator to adjust its rhythm to oscillate in phase via mutual coupling to other oscillators or being driven by an external signal [8,9].

As controllable quantum systems blossom in recent decades [10–12], synchronization studies have also been extended to the quantum regime [13–21]. Several works focus on the quantum van der Pol (qvdp) oscillator [18,19,22–29]. Compared to its classical counterpart [30], the deterministic trajectory and the limit cycle becomes meaningless due to the quantum noise [18,19,27]. Nevertheless, the synchronization features can still be captured by evaluating the phase

preference of the quasiprobability distribution in the position-momentum space [18,19,26,27]. Meanwhile, inspired by the qvdP oscillator in the deep quantum regime where only a few discrete energy levels are involved [18,19,22,26], the synchronization of systems with finite Hilbert space has also been of interest. Raised by Roulet and Bruder, spin-1 systems were theoretically shown to be synchronizable [31–33], and the experimental demonstrations were carried out subsequently [34,35]. Here, the limit cycle and synchronization can be generalized to spin systems by introducing the spin coherent states and Husimi- $Q$  representation [31,36]. The emergence of coherence between different energy levels induced by the external signal can be also interpreted as a sign of phase synchronization [33], providing a fresh understanding of quantum synchronization.

However, Ref. [31] also stated that quantum synchronization is not applicable for a single qubit (spin-1/2 system) due to the lack of the limit cycle [37]. It contradicts the fact that the qvdP oscillator can be synchronized at the quantum limit, where only the ground and the first-excited states are occupied [18,19,22]. Parra-López and Bergli solved this seeming conflict theoretically, showing that the limit cycle of a single qubit can be obtained by choosing appropriate pure states to construct mixed states (see Fig. 1) [38]; thus, a single qubit is certainly synchronizable. The debate on whether qubits can be synchronized is not only of academic interest; being able to synchronize qubits holds promise for potential applications of quantum synchronization in quantum information [16,39,40].

In this work, we experimentally demonstrate that a qubit can be synchronized with an external driving signal by

\*These authors contributed equally to this work.

†Jianwen.Jie1990@gmail.com

‡luy7@sustech.edu.cn

Published by the American Physical Society under the terms of the [Creative Commons Attribution 4.0 International](https://creativecommons.org/licenses/by/4.0/) license. Further distribution of this work must maintain attribution to the author(s) and the published article's title, journal citation, and DOI.

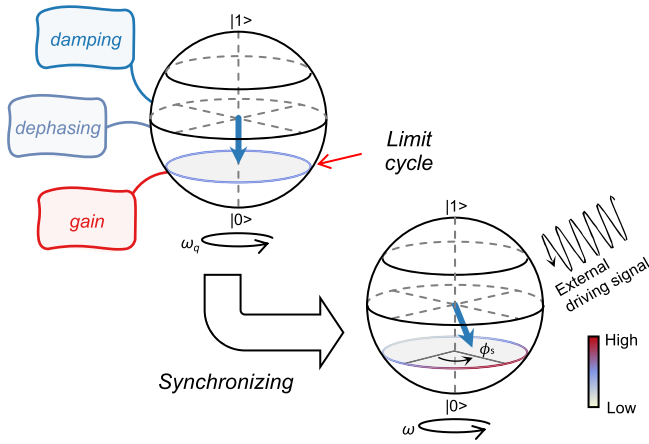


FIG. 1. Visualizing limit cycle and synchronization on the Bloch sphere. A qubit suffered from dissipations of *gain*, *damping*, and *dephasing* would finally evolve into a steady state. A limit cycle can be constructed from this steady state, by mixing pure states in the latitude circle with equal weights (uniform blue circle in the left sphere). All these states precess at the intrinsic frequency of  $\omega_q$ . After synchronization, the qubit obtains a phase preference  $\phi_s$  and precesses at the sync frequency  $\omega$ . The blue arrows indicate the Bloch vectors of the corresponding qubit states.

utilizing a trapped-ion system. We provide a clear characterization of the limit cycle, supply strong evidence of synchronization and ascertain the parameter intervals within which synchronization can be achieved. Our results are in remarkable quantitative agreement with theoretical predictions, showcasing trapped-ion systems as an excellent platform for further studies and applications of quantum synchronization. In the following content, we would first review the theory of synchronizing a single dissipated qubit in Sec. II and elucidate how synchronization can be characterized. We then present our experimental implementation in Sec. III. We would introduce our setup and key observations such as phase locking, frequency entrainment, and Arnold tongue. Next in Sec. IV, we would discuss an alternative method to investigate the limit cycle of single qubit through its classical motion in phase space. Finally, we would present our conclusion and outlook in Sec. V.

## II. THEORY ON QUBIT SYNCHRONIZATION

Hereby we first briefly review the theory of qubit synchronization. Specifically, we investigate a dissipated qubit perturbed by an external classical signal (referred to the sync signal in following) [38]. The qubit is described by the Hamiltonian  $\hat{H}_q = \omega_q \hat{\sigma}_z / 2$ , where  $\omega_q$  represents its energy gap. The sync signal driving the qubit is given by  $\hat{H}_d = \epsilon \cos(\omega t + \varphi) \hat{\sigma}_x$ , with  $\epsilon$ ,  $\omega$  and  $\varphi$  denoting the strength, frequency and initial phase of the signal, respectively. Here,  $\hat{\sigma}_{x,y,z}$  are Pauli operators. The dynamics of this system is governed by the following Lindblad equation:

$$\frac{d\hat{\rho}}{dt} = -\frac{i}{2}[\Delta\hat{\sigma}_z + \epsilon\hat{\sigma}_\varphi, \hat{\rho}] + \frac{\Gamma_g}{2}\mathcal{D}[\hat{\sigma}_+] \hat{\rho} + \frac{\Gamma_d}{2}\mathcal{D}[\hat{\sigma}_-] \hat{\rho} + \frac{\Gamma_z}{2}\mathcal{D}[\hat{\sigma}_z] \hat{\rho}, \quad (1)$$

where  $\hat{\sigma}_\varphi = \hat{\sigma}_x \cos \varphi + \hat{\sigma}_y \sin \varphi$ ,  $\Delta = \omega - \omega_q$ , and  $\hat{\rho}$  represents the density operator of the qubit. Note that the rotating frame together with the rotating wave approximation has been taken with respect to the frame of  $\hat{U}_{\text{sync}} = e^{-i\omega\hat{\sigma}_z t/2}$ . The Lindblad operators,  $\mathcal{D}[\hat{A}]\hat{\rho} = \hat{A}\hat{\rho}\hat{A}^\dagger - \{\hat{A}^\dagger\hat{A}, \hat{\rho}\}/2$ , describe the qubit dissipation, while  $\Gamma_g$ ,  $\Gamma_d$ , and  $\Gamma_z$  represent the gain, damping, and dephasing rates, respectively. As one of the standard approaches for studying quantum spin systems, we can translate the above master equation into the Bloch representation, resulting in the following set of equations:

$$\begin{aligned} \dot{m}_x &= -\frac{\Gamma_t m_x}{4} - \Delta m_y + \epsilon \cos \varphi m_z, \\ \dot{m}_y &= -\frac{\Gamma_t m_y}{4} + \Delta m_x + \epsilon \sin \varphi m_z, \\ \dot{m}_z &= \frac{\Gamma_g - \Gamma_d}{2} - \frac{\Gamma_g + \Gamma_d}{2} m_z \\ &\quad - \epsilon \cos \varphi m_x - \epsilon \sin \varphi m_y. \end{aligned} \quad (2)$$

Here,  $\mathbf{m} = \{m_x, m_y, m_z\}$  represents the Bloch vector with  $m_i = \text{Tr}[\hat{\sigma}_i \hat{\rho}]$ , and  $\Gamma_t$  is equal to  $\Gamma_g + \Gamma_d + 4\Gamma_z$ . When the sync signal is absent (indicating  $\epsilon = 0$ ), the above Bloch equations yield a stationary solution as follows,

$$\mathbf{m}_{\text{LC}} = \left\{ 0, 0, \frac{\Gamma_g - \Gamma_d}{\Gamma_g + \Gamma_d} \right\}. \quad (3)$$

Alternatively, in the eigenbasis of  $\hat{\sigma}_z$ , denoted as  $|0\rangle, |1\rangle$ , this stationary state can also be represented as

$$\rho_{\text{LC}} = \frac{\Gamma_d}{\Gamma_g + \Gamma_d} |0\rangle\langle 0| + \frac{\Gamma_g}{\Gamma_g + \Gamma_d} |1\rangle\langle 1|, \quad (4)$$

It is worth noting that there is seemingly no free phase if we simply treat the above stationary state in the eigenbasis of  $\hat{\sigma}_z$ . It previously led to a mistaken belief that a single dissipated qubit does not exhibit a limit cycle and therefore cannot be synchronized [31].

However, the conclusion turns out to be different if we choose an overcomplete set of coherent-spin states (CSSs) defined as follows:

$$|\theta, \phi\rangle = e^{-i\phi\hat{\sigma}_z/2} e^{-i\theta\hat{\sigma}_y/2} |1\rangle. \quad (5)$$

It corresponds to the eigenstate of the operator  $\mathbf{n}_{\theta,\phi} \cdot \hat{\sigma}$  and  $\mathbf{n}_{\theta,\phi} = \{\sin \theta \cos \phi, \sin \theta \sin \phi, \cos \theta\}$ . With this basis, the stationary state given in Eq. (4) can be rewritten as

$$\rho_{\text{LC}} = \frac{1}{2\pi} \int_0^{2\pi} d\phi |\theta_0, \phi\rangle\langle \theta_0, \phi|, \quad (6)$$

where

$$\theta_0 = \arccos\left(\frac{\Gamma_g - \Gamma_d}{\Gamma_g + \Gamma_d}\right). \quad (7)$$

Obviously, this stationary state Eq. (4) can be treat as an ensemble of CSSs with the same energy (see Fig. 1), and since the CSS with different phase  $\phi$  contribute equally to the state, it is appropriate to consider  $\phi$  as a free phase. Consequently, this stationary state can be interpreted as the limit cycle of the dissipated qubit.

Additionally, similar to the Wigner representation utilized in oscillator systems, we introduce the Husimi- $Q$

representation ( $Q$  function) [36],

$$Q(\theta, \phi) = \frac{1}{2\pi} \langle \theta, \phi | \hat{\rho} | \theta, \phi \rangle, \quad (8)$$

to represent the quasiprobability distribution of any qubit state in the phase portrait of the Bloch sphere. In this representation, the limit cycle state reads as follows:

$$Q(\theta, \phi) = \frac{1}{4\pi} (1 + m_{\text{LC},z} \cos \theta), \quad (9)$$

which displays a uniform quasiprobability distribution along the longitude axis.

Now we consider the case where the external signal is applied to the dissipated qubit. The Bloch equations Eq. (2) yield a stationary solution as follows:

$$\begin{aligned} m_x &= \frac{4\epsilon(\Gamma_g - \Gamma_d)(4\Delta \cos \phi + \Gamma_t \sin \phi)}{(16\Delta^2 + \Gamma_t^2)(\Gamma_g + \Gamma_d) + 8\Gamma_t\epsilon^2}, \\ m_y &= \frac{4\epsilon(\Gamma_g - \Gamma_d)(4\Delta \sin \phi - \Gamma_t \cos \phi)}{(16\Delta^2 + \Gamma_t^2)(\Gamma_g + \Gamma_d) + 8\Gamma_t\epsilon^2}, \\ m_z &= \frac{(16\Delta^2 + \Gamma_t^2)(\Gamma_g - \Gamma_d)}{(16\Delta^2 + \Gamma_t^2)(\Gamma_g + \Gamma_d) + 8\Gamma_t\epsilon^2}. \end{aligned} \quad (10)$$

To characterize the performance of synchronization, we utilize the *synchronization measurement* ( $S$ function) defined as [31,38]

$$\begin{aligned} S(\phi) &= \int_0^\pi d\theta Q(\theta, \phi) \sin \theta - \frac{1}{2\pi} \\ &= \frac{1}{8} (m_x \cos \phi + m_y \sin \phi). \end{aligned} \quad (11)$$

Obviously, the synchronization measurement gives rise to  $S(\phi) = 0$  for the unsynchronized limit cycle state. While the qubit state is synchronized, the  $S$  function would show a nonuniform distribution over  $\phi$ .

For the qubit subjected to an external signal, we can analytically obtain the  $S$ -function by inserting Eq. (10) into Eq. (11) and the result yields as follows:

$$S(\phi) = \frac{\mathcal{C}}{2} \sin(\phi + \phi_d - \phi), \quad (12)$$

where the contrast  $\mathcal{C}$  reads as

$$\mathcal{C} = \frac{\epsilon|\Gamma_g - \Gamma_d|}{(16\Delta^2 + \Gamma_t^2)(\Gamma_g + \Gamma_d) + 8\Gamma_t\epsilon^2} \sqrt{16\Delta^2 + \Gamma_t^2}, \quad (13)$$

and the additional phase shift  $\phi_d$  is

$$\phi_d = \arctan \frac{4\Delta}{\Gamma_t}. \quad (14)$$

The contrast  $\mathcal{C}$  provides a suitable measure of synchronization performance, and the synchronized phase  $\phi_s$  can be determined as follows:

$$\phi_s = \begin{cases} \phi + \phi_d - \frac{\pi}{2}, & \Gamma_g > \Gamma_d \\ \phi + \phi_d + \frac{\pi}{2}, & \Gamma_g < \Gamma_d \end{cases}. \quad (15)$$

Note that the signatures of the synchronization are evaluated in the rotating frame to avoid directly measuring the fast oscillation of the qubit in the Schrodinger picture, which

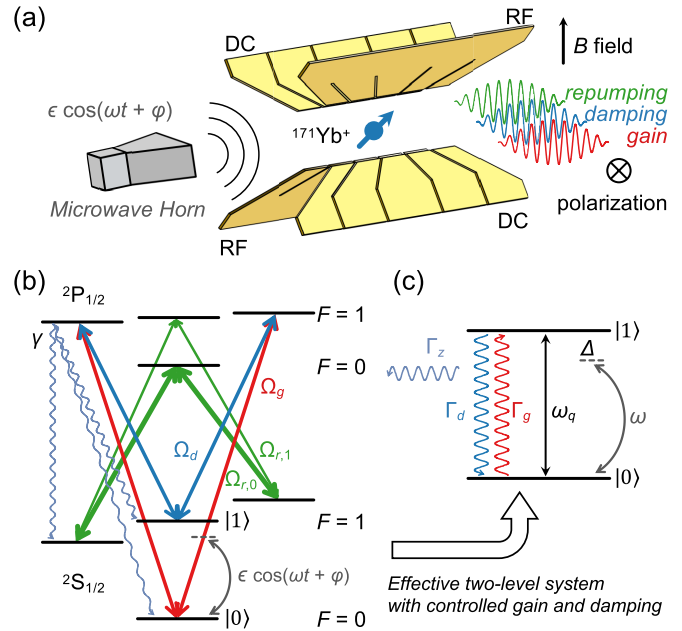


FIG. 2. (a) Experimental setup. A single  $^{171}\text{Yb}^+$  ion is held in a five-segmented blade-type Paul trap. Three beams, marked as gain, damping, and repumping are aligned to the ion, and all the polarizations are perpendicular to the static magnetic field. The external sync signal is broadcasted to the ion through a microwave horn. (b) Energy levels of  $^{171}\text{Yb}^+$  ion. The transitions driven by the gain (red), damping (blue), and repumping (green) beams are shown, with the coupling strengths of  $\Omega_g$ ,  $\Omega_d$ , and  $\Omega_{r,0/1}$ , respectively. For the spontaneous emission, we only show the decay channels from the  $^2P_{1/2} |F=1, m_F=-1\rangle$  level for clarity. (c) Dissipated qubit. Provided that  $\gamma \sim \Omega_{r,0} \gg \Omega_g, \Omega_d, \Omega_{r,1}$ , as is the case in our experiment, the whole system is well approximated by a two-level system with controlled gain and damping rates, which can be coherently driven by the sync signal.

are conventionally used in studying the synchronization of quantum spin systems [31–35]. Further discussion on qubit synchronization in the Schrödinger picture can be found in Appendix F.

### III. EXPERIMENTAL RESULTS

#### A. Setup

To experimentally demonstrate qubit synchronization, we utilize a trapped-ion system and employ a qubit encoded in a single  $^{171}\text{Yb}^+$  ion [see Fig. 2(a)]. Here, the qubit is represented by the hyperfine levels belonging to the ground manifold, denoted as  $|0\rangle \equiv ^2S_{1/2} |F=0, m_F=0\rangle$  and  $|1\rangle \equiv ^2S_{1/2} |F=1, m_F=0\rangle$ , with an energy gap of  $\omega_q/(2\pi)$  around 12.6 GHz [41], as shown in Fig. 2(b). The qubit can be initialized to the  $|0\rangle$  state via optical pumping, while the state measurement is performed by selectively exciting the  $|0\rangle$  level to the  $^2P_{1/2} |F=0\rangle$  levels and counting the emitting photons [42]. In our system, the state-preparation-and-measurement (SPAM) error is less than  $7 \times 10^{-3}$ . More details of the setup can be found in Appendix A.

To realize a dissipated qubit, we engineer the gain and damping processes in a fully controlled way [43,44], as illustrated in Figs. 2(b) and 2(c). More specifically, the

ion is driven from  $|0\rangle$  ( $|1\rangle$ ) to  ${}^2P_{1/2} |F=1, m_F=\pm 1\rangle$  at a coupling strength of  $\Omega_g$  ( $\Omega_d$ ), followed by a fast spontaneous emission to both  $|1\rangle$  and  $|0\rangle$ . The state leakage to  ${}^2S_{1/2} |F=1, m_F=\pm 1\rangle$  is quickly repumped back to the qubit space by strongly coupling these states to  ${}^2P_{1/2} |F=0, m_F=0\rangle$  and  ${}^2P_{1/2} |F=0, m_F=1\rangle$ . Taken together, these processes result in an incoherent gain (damping) at a rate of  $\Gamma_g$  ( $\Gamma_d$ ) within the qubit system, accompanied by a pure dephasing dynamics at a rate of  $\Gamma_z$ .

The dissipation rates of  $\Gamma_g$  and  $\Gamma_d$  can be independently tuned by adjusting the related lasers' power to change strengths of  $\Omega_g$  and  $\Omega_d$ , respectively, and the dephasing rate of  $\Gamma_z$  is determined afterwards. In the experiments, these rates are set by choosing appropriate coupling strengths and accurately measured. Further details can be found in Appendix B. A classical external signal (sync signal) with frequency  $\omega$ , strength  $\epsilon$  and initial phase  $\varphi = \pi/2$  is then broadcasted to the ion through a microwave horn [42]. All experimental results are compared to numerical simulations based on Eq. (1).

### B. Characterization of dissipated qubit

In our experimental setup, We first demonstrate the behavior of the dissipated ion qubit and concurrently evaluate all the dissipation rates. We perform independently measurements for the gain rate  $\Gamma_g$  and the damping rate  $\Gamma_d$  by initialize the qubit state to the  $|0\rangle$  and  $|1\rangle$  states, respectively, and then engineering only the gain or damping process. The summarized results are presented in Fig. 3(a). The measured values for the gain rate  $\Gamma_g$  and the damping rate  $\Gamma_d$  are  $(2\pi) \times 1.27(4)$  kHz and  $(2\pi) \times 7.33(11)$  kHz, respectively, based on the direct fitting results. The error bars here and below all represent standard deviation. These values give an anisotropic ratio  $\Gamma_d/\Gamma_g = 5.8$ . Note that, the synchronization can occur as long as  $\Gamma_g$  and  $\Gamma_d$  both nonidentical and nonzero [38]. Hence, our experimental settings are suitable for observing qubit synchronization. In Fig. 3(b), we also simultaneously engineer the gain and damping processes, and the measured decay rate of  $(2\pi) \times 8.59(39)$  kHz matches the value of  $\Gamma_g + \Gamma_d$  well.

To estimate the value of  $\Gamma_z$ , we initialize the initial qubit state to one eigenstate of  $\hat{\sigma}_x$  and then measure in the  $\hat{\sigma}_x$  basis as well, as depicted in Fig. 3(c). In this scenario, the decay rate is equal to  $2\Gamma_z + (\Gamma_g + \Gamma_d)/2$ , since the gain and damping processes can also induce dephasing in the qubit. Utilizing the previously obtained values of  $\Gamma_g$  and  $\Gamma_d$ , we have already obtained, we can estimate the value of pure dephasing  $\Gamma_z$  to be  $(2\pi) \times 4.42(106)$  kHz.

### C. Qubit synchronization to resonant signals

As the first examination, we demonstrate the situation that a dissipated qubit driven by a resonant external signal, and the experimental observations of the qubit synchronization are summarized in Fig. 4.

We prepare the qubit to the  $|1\rangle$  state and confirm that the undriven self-sustained qubit would relax to the limit cycle state under the dissipations. As shown in Fig. 4(a), after the first-stage evolution lasting  $200 \mu\text{s}$ , the qubit has reached the limit cycle described by the Bloch vector of  $\mathbf{m}_{\text{LC}}^{(\text{exp})} = \{0, 0, -0.700(16)\}$ , which is consistent with

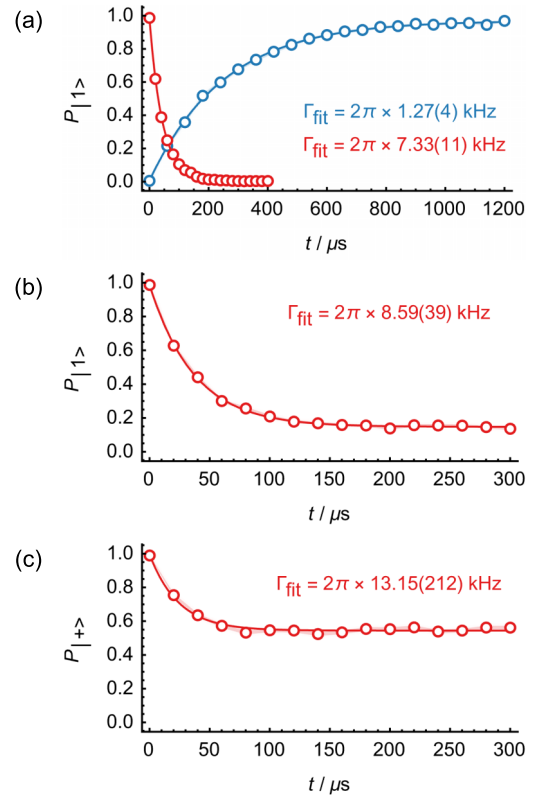


FIG. 3. Experimental results of measuring decay rates. The blue and red lines (points) in (a) represent the results for pure gain and pure damping processes, respectively. In (b), both gain and damping processes are engineered simultaneously. The initial state is prepared in the  $|1\rangle$  state, and then it is measured in the  $\sigma_z$  basis. In (c), we initialize the qubit state to  $|+\rangle = (|1\rangle + |0\rangle)/\sqrt{2}$  and then measure the decay of qubit coherence, referring to the value of  $2\Gamma_z + (\Gamma_g + \Gamma_d)/2$ . In all these cases, a fit function of  $Ae^{-\Gamma t/2} + B$  is used to extract the decay rate  $\Gamma_{\text{fit}}$  for each figure. The open markers and the shaded lines represent the experimental results and the standard deviations, respectively, while the solid red lines indicate the fitting results.

the predicted value of  $\mathbf{m}_{\text{LC}}^{(\text{th})} = \{0, 0, (\Gamma_g - \Gamma_d)/(\Gamma_g + \Gamma_d)\} = \{0, 0, -0.705\}$ . The limit cycle can be further visualized by utilizing the Husimi- $Q$  representation described by Eq. (8). The  $Q$  functions of the initial and limit cycle states are experimentally measured, as illustrated in Figs. 4(b) and 4(c). The contribution to the limit cycle mainly comes from the pure states near the south pole of the Bloch sphere, due to the anisotropic ratio  $\Gamma_d/\Gamma_g > 1$ . The preference in the phase  $\phi$  of any state can be evaluated by the *synchronization measurement* defined by Eq. (11). The values of  $S$  function for the initial and limit cycle states are also shown in Figs. 4(b) and 4(c). The initial state shows a weak phase preference around  $1.48(2)\pi$  due to the imperfect state preparation, while for the limit cycle this preference completely vanishes as it should.

After the qubit reaches at the limit cycle, we apply a resonant sync signal ( $\Delta \sim 0$ ) with strength  $\epsilon = (2\pi) \times 2.37(1)$  kHz ( $\epsilon/\Gamma_g = 1.87$ ). In Fig. 4(a), the qubit has reached the final synchronized state after another  $200 \mu\text{s}$  evolution. As a sign of synchronization, a nonzero value is observed in  $m_x$ ,



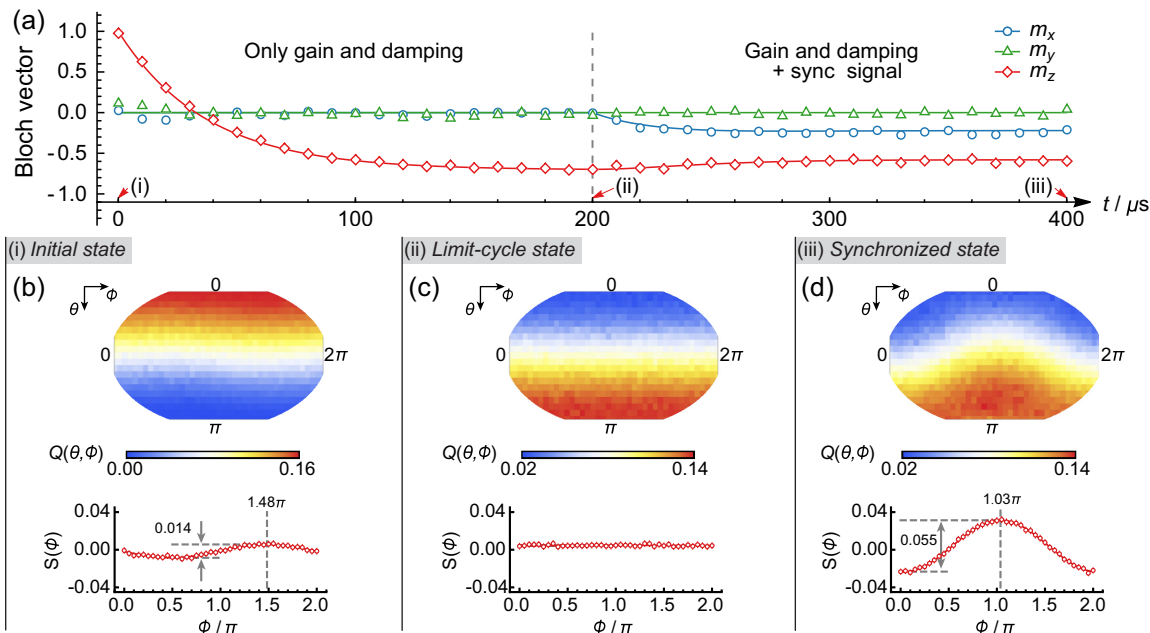


FIG. 4. Experimental results of quantum synchronization. (a). Time evolution of the Bloch vector. From 0 to 200  $\mu\text{s}$ , only gain and damping processes are engineered to establish the limit cycle. Subsequently from 200 to 400  $\mu\text{s}$ , the sync signal is triggered simultaneously to synchronize the qubit to the signal. Here and in the following figures, the open markers represent the experimental results, while the error bars of a standard deviation are smaller than the size of the markers. The solid lines represent numerical simulation results. To verify the achievements of the limit cycle and the synchronized state, we measure the  $Q$  functions and also the  $S$  functions at the time of (i)  $t_0 = 0 \mu\text{s}$ , (ii)  $t_1 = 200 \mu\text{s}$ , and (iii)  $t_1 + t_2 = 400 \mu\text{s}$ , which correspond to the initial, limit cycle and synchronized state, respectively. [(b)–(d)] shows the results of the  $Q$  function under the Winkel triplel projection (first row) and the  $S$  function (second row) for the time of (i)–(iii), respectively.

indicating that the sync signal rebuilds the qubit coherence. For further verification, we also measure the  $Q$  and  $S$  functions for the synchronized state, as shown in Fig. 4(d). The phase preference reappears at  $\phi = 1.03(2)\pi$ , since we set  $\Gamma_d > \Gamma_g$  and the sync signal phase to be  $\pi/2$  (as claimed in Sec. II). The fitting contrast of the  $S$  function reaches 0.055(1), significantly deviating from the unsynchronized limit cycle. The above results indicate the experimental achievement of synchronization with anti-phase locking. Note that the methods to obtain the  $Q$  and  $S$  functions in experiments are discussed in Appendix C.

#### D. Synchronization region over different signal frequencies and amplitudes

Now we tune the sync frequency away from the qubit frequency ( $\Delta \neq 0$ ) while leaving the sync strength  $\epsilon$  unchanged to investigate the frequency entrainment. Figure 5(a) clearly shows that the qubit can be synchronized for a wide range of the sync signal frequency but with a delay or advance in the locked phase [see Fig. 5(b)]. Such phase shift might provide an alternative approach to sense the drift in magnetic field strength by employing a magnetic-field-sensitive qubit.

In addition to the locked phase shift, the maximal value of the synchronization measurement,  $\text{Max}[S(\phi)]$ , also degrades with increasing detuning  $\Delta$ . As an example shown in Fig. 5(c), the value of  $\text{Max}[S(\phi)]$  drops by half when the detuning  $\Delta$  increases to  $10.7\Gamma_g$ , under the sync strength of  $\epsilon = 1.87\Gamma_g$ . This frequency bandwidth strongly depends on the sync strength; therefore, we measure the value of  $\text{Max}[S(\phi)]$  across a wide

range of the sync detuning and strength, as shown in Fig. 5(d). This result is known as the *Arnold tongue* [8]. It is remarkable that synchronization occurs as long as the sync strength is nonzero, regardless of how weak it is. However, weak signals result in small maximal values in the  $S$  function, making the synchronization hard to be distinguished from the noisy fluctuation in practice.

The limit cycle can also be distorted by sync signals that are too strong. The deformation of the limit cycle can be characterized by [33]

$$p_{\text{deform}}(\epsilon) = \text{Tr}[\hat{\sigma}_z(\hat{\rho}_{\text{syn}}(\epsilon) - \hat{\rho}_{\text{syn}}(0))], \quad (16)$$

where  $\hat{\rho}_{\text{syn}}(\epsilon)$  is the density matrix of the synchronized state under the sync strength of  $\epsilon$ , and  $\hat{\rho}_{\text{syn}}(0)$  indicates the limit cycle. We experimentally measure the deformation with the resonant sync signal, shown in Fig. 6(a). The deformation increases as the sync strength gets stronger, and eventually saturates to  $p_{\text{deform}}^{(\text{sat})} = -m_{\text{LC},z}$ . The saturation indicates that the Bloch vector of the qubit state lies on the  $x$ - $y$  plane of the Bloch sphere, and the limit cycle established by the gain and damping is fully distorted. This matches the results of the corresponding  $S$  function measurement in Fig. 6(b). We find that the phase preference becomes first more pronounced as the sync strength increases and then gradually weakens when the signal becomes too strong. Thus there is generally a trade-off between the distortion in the limit cycle and the sensitivity of the phase preference, which should be carefully balanced in practical implementations.

We have further checked the time evolution of the qubit starting from the limit cycle state but under different sync

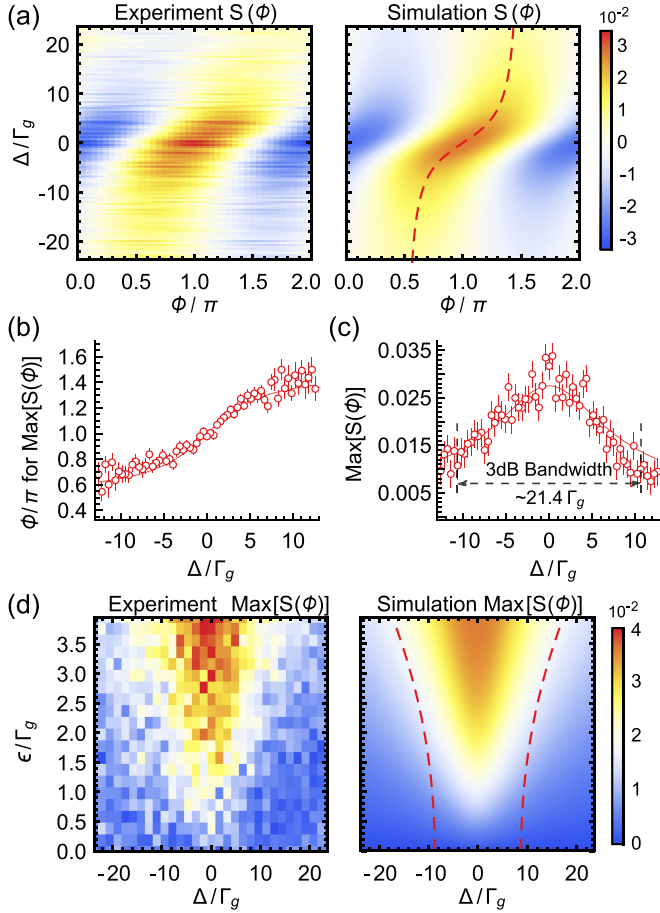


FIG. 5. (a) Synchronization under detuned sync signals. Here the sync strength is kept at  $\epsilon = 1.87\Gamma_g$ . The experimental results (left) agree well with simulations (right). The synchronization performs the best under the resonant situation and can be achieved across a wide range of sync frequency. (b) Shift in locked phase. The numerical simulation results correspond to those along the red-dashed in the right sub-figure of (a). (c) Frequency bandwidth of synchronization. A 3 dB bandwidth of  $21.4\Gamma_g$  is obtained at the sync strength of  $\epsilon = 1.87\Gamma_g$ . (d) Arnold tongue. The left and right sub-figures correspond to the experimental and the simulation results. The red dashed lines in the right subfigure indicate the 3 dB frequency bandwidth of the synchronization under different sync strengths.

strengths, as illustrated in Fig. 6(c). The significant oscillation of the system energy is observed when the sync strength approaches  $28.7\Gamma_g$ , and the fitting result gives the oscillating frequency of  $27.7(6)\Gamma_g$ . This result clearly indicates that the qubit is forcibly driven by the too strong signal, instead of synchronizing to it. Note that the time evolution of all Bloch components at synchronization strengths of  $3.75\Gamma_g$  and  $28.7\Gamma_g$  is presented in Appendix D.

#### IV. DISCUSSION ON LIMIT CYCLE

In previous studies [31,38], the analysis regarding the existence of a limit cycle always relied on steady quantum states of the dissipated spin system and the quasiprobability distribution in the Husimi- $Q$  representation. This approach may lead to misconceptions, such as the belief that a single

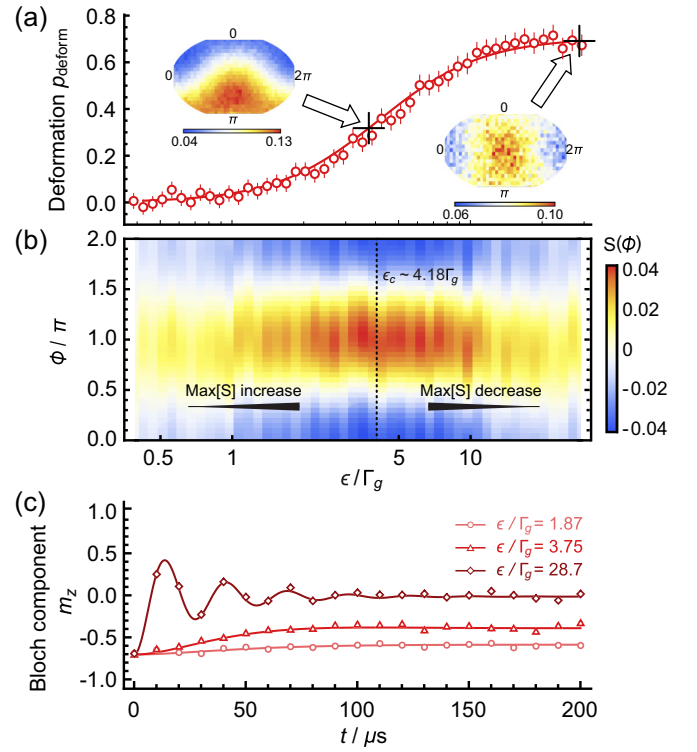


FIG. 6. Performance of synchronization under resonant driving with different sync strengths. (a) Deformation of limit cycle. The synchronized state departs from the limit-cycle state as the sync strength increases. The left and right inset figures indicate the  $Q$  functions with the sync strength  $\epsilon$  of  $3.75\Gamma_g$  and  $28.7\Gamma_g$ , respectively. (b) Synchronization measurement under different sync strengths. The maximal value of the  $S$  function increases at first, and then after a critical value of  $\epsilon_c$  it tends to drop back to zero. Under our setting parameters, the critical sync amplitude is around  $4.18\Gamma_g$ . (c) Time evolution of Bloch vector component  $m_z$  starting from the limit cycle state. Under the sync strengths of  $1.87\Gamma_g$  and  $3.75\Gamma_g$ , the system evolves almost smoothly to the final steady state, while with the strength of  $28.7\Gamma_g$ , the system significantly oscillates before fully decay.

qubit cannot be synchronized. Here, we attempt to adopt an alternative approach. By establishing evolution equations that describe the “classical motion” of the qubit in the phase space, we investigate whether a single dissipated qubit can own a valid limit cycle. This method is quite similar to that utilized in studying synchronization of quantum oscillators [18,26,29].

To start, we derive the evolution equations for the Pauli operators in the Heisenberg picture as follows:

$$\begin{aligned}
 \frac{d\langle\hat{\sigma}_x\rangle}{dt} &= -\frac{\Gamma_t}{4}\langle\hat{\sigma}_x\rangle - \omega_q\langle\hat{\sigma}_y\rangle, \\
 \frac{d\langle\hat{\sigma}_y\rangle}{dt} &= -\frac{\Gamma_t}{4}\langle\hat{\sigma}_y\rangle + \omega_q\langle\hat{\sigma}_x\rangle \\
 &\quad - 2\epsilon\cos(\omega t + \varphi)\langle\hat{\sigma}_z\rangle, \\
 \frac{d\langle\hat{\sigma}_z\rangle}{dt} &= \frac{\Gamma_g - \Gamma_d}{4} - \frac{\Gamma_g + \Gamma_d}{4}\langle\hat{\sigma}_z\rangle \\
 &\quad + 2\epsilon\cos(\omega t + \varphi)\langle\hat{\sigma}_y\rangle. \tag{17}
 \end{aligned}$$

For quantum oscillators, we could obtain the “classical trajectory” by approximating the value of  $\langle \hat{a} \rangle$  to be

$$\langle \hat{a} \rangle = \text{Tr}[\hat{a}\hat{\rho}] \rightarrow \alpha = \text{Tr}[\hat{a}|\alpha\rangle\langle\alpha|]. \quad (18)$$

Here,  $\hat{a}$  is the annihilation operator of the quantum harmonic oscillator, and the coherent states  $|\alpha\rangle$  are treated as the “most classical” quantum states. The evolution of  $\alpha$  is regarded as the “classical trajectory.” Similarly, in the qubit system, we attempt to employ the coherent-spin states  $|\theta, \phi\rangle$  to obtain the corresponding classical motion. By utilizing the approximation of  $\langle \hat{\sigma}_k \rangle \rightarrow \text{Tr}[\hat{\sigma}_k|\theta, \phi\rangle\langle\theta, \phi|]$ , we have the following relationships:

$$\begin{aligned} \langle \hat{\sigma}_x \rangle &\rightarrow \cos \phi \sin \theta, \\ \langle \hat{\sigma}_y \rangle &\rightarrow \sin \phi \sin \theta, \\ \langle \hat{\sigma}_z \rangle &\rightarrow \cos \theta. \end{aligned} \quad (19)$$

Intuitively, it works like tracking the pointing direction (latitude  $\theta$  and longitude  $\phi$ ) of a classical spin, therefore the Bloch vector is kept being normalized and projected onto the surface of the Bloch sphere during the evolution. By inserting the above relations into the Heisenberg equations of the qubit, we could derive the time evolutions of  $\theta$  and  $\phi$  as follows:

$$\begin{aligned} \frac{d\theta}{dt} &= \frac{\Gamma_d}{2}(\cot \theta + \csc \theta) + \frac{\Gamma_g}{2}(\cot \theta - \csc \theta) \\ &\quad - 2\epsilon \cos(\omega t + \varphi) \sin \phi \\ \frac{d\phi}{dt} &= \omega_q \phi - 2\epsilon \cot \theta \cos(\omega t + \varphi) \cos \phi. \end{aligned} \quad (20)$$

Remarkably, we find that the above equations are quite similar to those of quantum oscillators, where  $\theta$  can be appropriately interpreted as the oscillation amplitude of the qubit.

By solving the equation for  $\theta$  when the external signal is absent, we could obtain the steady-state solution as follows:

$$\begin{aligned} \theta_{\text{steady}} &= \arccos\left(\frac{\Gamma_g - \Gamma_d}{\Gamma_g + \Gamma_d}\right) \\ &= \begin{cases} \pi/2 & \text{if } \Gamma_g = \Gamma_d \\ 0 & \text{if } \Gamma_d = 0 \\ \pi & \text{if } \Gamma_g = 0 \\ \text{finite value} & \text{all other cases} \end{cases}. \end{aligned} \quad (21)$$

Starting from the steady state and triggering the external signal, the strength of the phase response is proportional to  $2\epsilon \cot \theta_{\text{steady}}$ , which can be further expressed as

$$2\epsilon \cot \theta_{\text{steady}} = \begin{cases} 0 & \text{if } \Gamma_g = \Gamma_d \\ \text{infinity} & \text{if } \Gamma_d = 0 \\ \text{infinity} & \text{if } \Gamma_g = 0 \\ \text{finite value} & \text{all other cases} \end{cases}. \quad (22)$$

For the case of  $\Gamma_g = \Gamma_d$ , as already clarified in Sec. II, this type of dissipated qubit cannot be synchronized. Here, we further provide more evidence that if  $\Gamma_g = \Gamma_d$ , the oscillation phase has no response to the external signal, regardless of its strength. In addition to this case, in Ref. [38], Parra-López and Bergli also claim that the qubit cannot be synchronized if either  $\Gamma_d$  or  $\Gamma_g$  is zero. We can note that according to Eq. (22) the oscillation phase would respond instantaneously to the external signal in these cases. Therefore, instead of

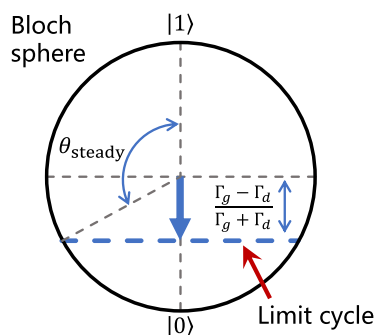


FIG. 7. Express a valid limit cycle on the Bloch sphere. The limit cycle obtained by solving the classical trajectory is exactly the same as that shown in Fig. 1.

synchronization, the qubit is forced by the external signal. Thus, for these two cases, we could also conclude that the dissipated qubit is unsynchronizable. Such behavior is similar to that of the quantum damped oscillator (see in Appendix E), which cannot be synchronized as well. The physical interpretation is also straightforward. When the gain rate  $\Gamma_g$  (damping rate  $\Gamma_d$ ) is zero, the qubit state would relax to the  $|0\rangle$  ( $|1\rangle$ ) state, corresponding to a fixed point on the surface of the Bloch sphere. Thus the qubit does not exhibit a valid limit cycle.

Now we turn to the case that  $\Gamma_g$  and  $\Gamma_d$  have nonidentical values and neither of them is zero. In these cases, the steady state of the oscillation amplitude  $\theta_{\text{steady}}$  has a finite value if the external signal is absent, and the oscillation phase is fully free. When the external signal is triggered, the oscillation phase  $\phi$  responds to the external signal with a finite strength  $2\epsilon \cot \theta_{\text{steady}}$  as well. These behaviors are exactly the same as those of the quantum vdP oscillator (see also in Appendix E). Thus we can conclude that this type of dissipated qubit performs like the quantum vdP oscillator and is synchronizable.

The value of  $\theta_{\text{steady}}$  has a clear meaning in the Bloch sphere representation, as illustrated in Fig. 7. The steady solution  $\theta_{\text{steady}}$  obtained by solving the equations of classical motion is well corresponds to the value of  $\theta_0$  in Eq. (7).

As an example, we illustrate the time evolution of the “classical trajectories” of the dissipated qubit in the phase space, and all the numerical results are shown in Fig. 8. To clearly display the limit cycle, the phase space is transformed from polar coordinates  $|\theta, \phi\rangle$  to normalized rectangular coordinates of  $\{(1 + \cos \theta) \cos \phi/2, (1 + \cos \theta) \sin \phi/2\}$ . The subfigures in the first row illustrates the evolution of the system under only dissipation with random initial states. It is evident that all the states evolve onto a circle with a finite radius of  $(1 + \cos \theta_{\text{steady}})/2$ . Later, when the external signal is triggered, we find that all the states tend to oscillate in phase progressively, indicating the process of synchronization.

In addition, we want to point that a value of  $\pi$  for  $\theta_{\text{steady}}$  in the case of  $\Gamma_g = 0$ , seems to be the cycle with the largest radius, it does not represent a valid limit cycle. Since for the coherent-spin states  $|\theta, \phi\rangle$ , it turns out to have the relation of  $|\theta = \pi, \phi\rangle = |0\rangle$ . Therefore the seeming cycle in the phase space for the case of  $\Gamma_g = 0$  is in fact equivalent to a single point. Thus for  $\Gamma_g = 0$ , the dissipated qubit does not hold a

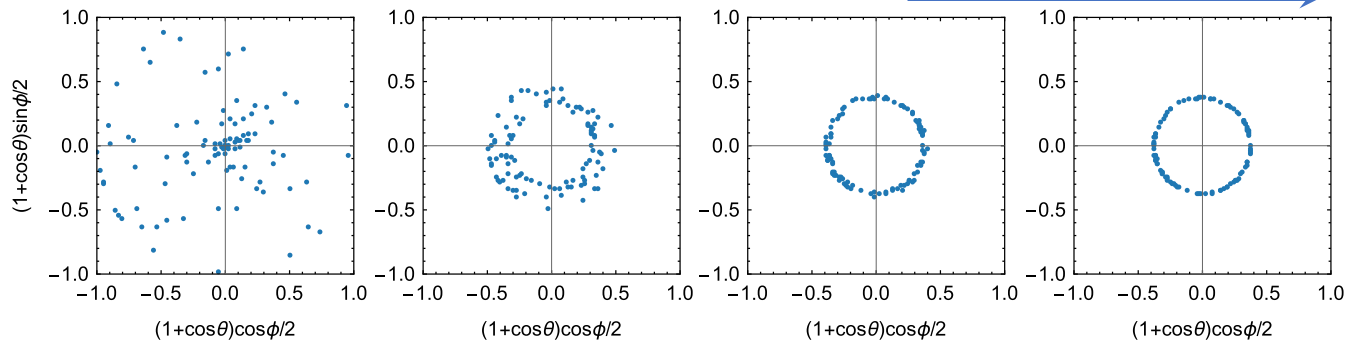
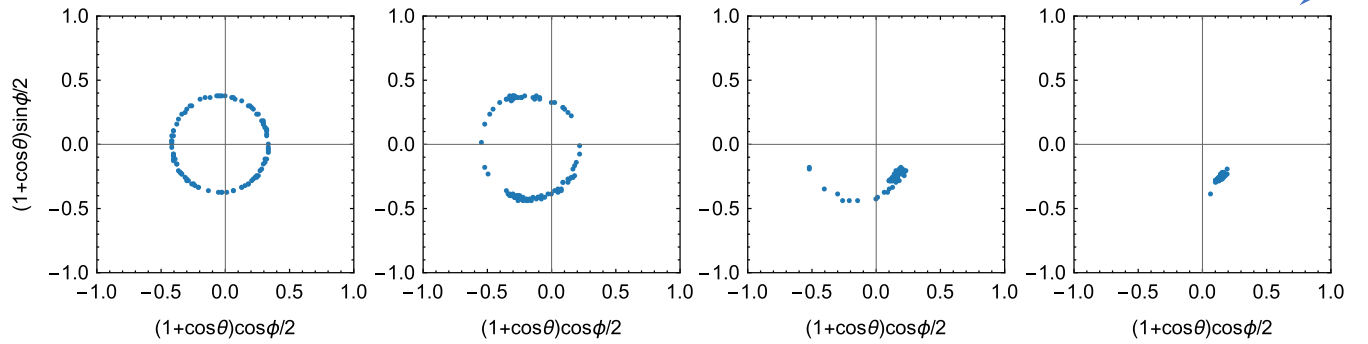
Without external signal  $\epsilon = 0$ With external signal  $\epsilon \neq 0$ 

FIG. 8. Classical trajectories of the dissipated qubit in the phase space. Each spot represents the evolution from one random initial state. Here we choose the ratio between the damping and the gain rates to be  $\Gamma_d/\Gamma_g = 5/3$  to clearly visualize the limit cycle.

valid limit cycle as well. Moreover, the “classical trajectory” method could be applied to the spin-1 system, and the obtained results are consistent with the analysis presented by Roulet and Bruder [31].

## V. CONCLUSION

We have realized the synchronization between an ion qubit and an external driving signal, and clear evidence of phase synchronization and frequency entrainment has been observed. The methods developed here can be extended to various platforms, such as neutral atoms and superconducting qubits, making it possible to synchronize hybrid systems with proper frequency conversion.

Future research should further consider synchronization in multi-qubits systems, as well as finding practical applications. For instance, qubits synchronized to the same signal can be treated as a homogeneous spin ensemble, and such ensembles in quantum magnetic could be helpful to generate phase-correlated magnetic fields and enhance quantum sensing [40]. For quantum memories in solid-state systems, the memory qubits inevitably couple to the environmental qubits with random phases and strengths [45]. Synchronizing environmental qubits might effectively suppress the randomness imparted to memory qubits, thereby prolonging their coherent storage time. Recent research also widely considers utilizing dissipations as resources for quantum information [46,47], and quantum synchronization offers one fresh and promising route for applications of dissipative quantum engineering.

## ACKNOWLEDGMENTS

We gratefully thank Dapeng Yu for providing critical support to this project. We also thank Junqiu Liu for carefully reading this manuscript and Fudong Wang for the helpful discussions on quantum memory. This work was supported by the National Science Foundation of China (Grants No. 12004165, No. 12104210), Shenzhen Science and Technology Program (Grants No. RCBS20200714114820298, No. ZDSYS20200811143600001), Guangdong Basic and Applied Basic Research Foundation (Grant No. 2022B1515120021), China Postdoctoral Science Foundation (Grant No. 2022M711496), Guangdong Provincial Key Laboratory (Grant No. 2019B121203002). Z-G.W. acknowledges support from the National Science Foundation of China (Grant No. 11974161) and Shenzhen Science and Technology Program (Grant No. KQTD20200820113010023). Y.W. acknowledges support from the National Science Foundation of China (Grant No. 12104205). Z.W. acknowledges support from the National Natural Science Foundation of China (Grant No. 11904423) and the Guangdong Basic and Applied Basic Research Foundation (Grant No. 2020A1515010864).

## APPENDIX A: EXPERIMENTAL SETUP

As a supplement, we show more details of our setup in Fig. 9. A single ytterbium ion is captured in a trap with frequencies of approximately  $\{v_x, v_y, v_z\} = 2\pi \times \{2.8, 2.2, 0.5\}$  MHz. For  $^{171}\text{Yb}^+$ , the resonant wavelength between its ground state  $^2S_{1/2}$  and the excited state  $^2P_{1/2}$  is about



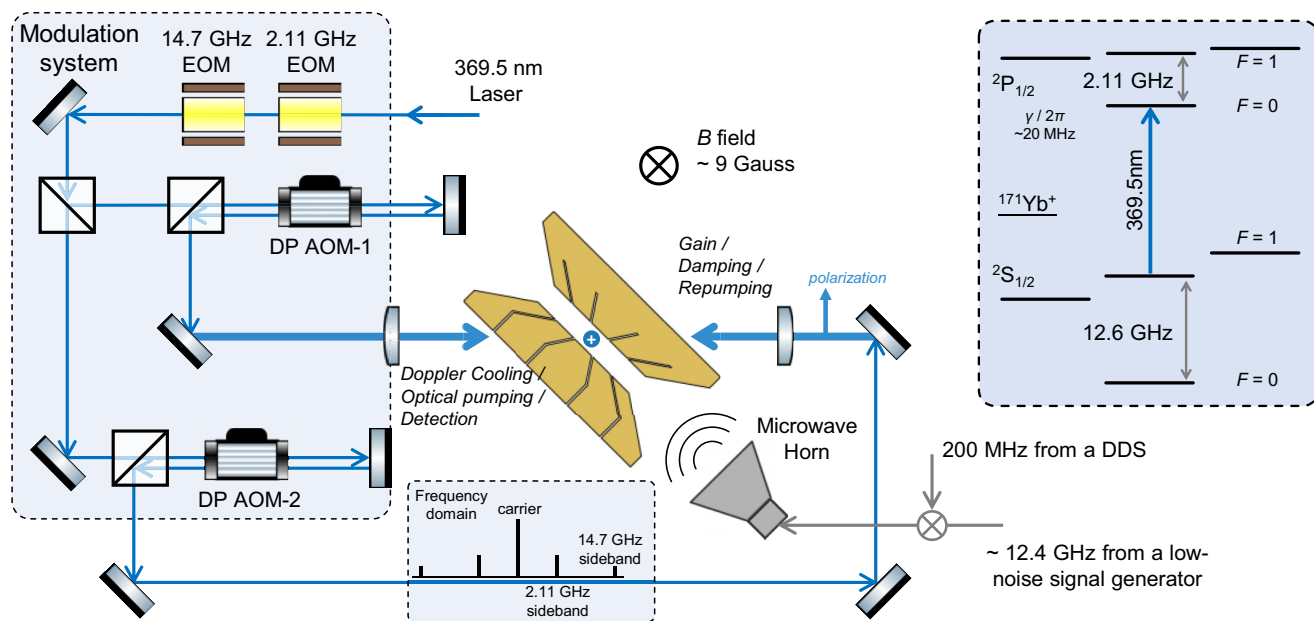


FIG. 9. Experimental setup. A single ion is trapped in the blade-type Paul trap. A 369.5 nm laser beam, which drives the main transition between the  $^2S_{1/2}$  and  $^2P_{1/2}$  levels (as shown in the upper-right inset figure), goes through a modulation system and then aligned to the ion position, to realize all the operations required in the experiments. A static magnetic field  $B$  around 9 Gauss is set to define the quantization axis and lift the energy degeneracy of the Zeeman levels as well. The external driving signal, which is broadcasted to the ion through the microwave horn, is generated by mixing a fixed microwave signal (around 12.4 GHz) from a ultra low-noise signal generator with a tunable radiofrequency signal (around 200 MHz) from a direct digital synthesis board (DDS).

369.5 nm. To cover all the hyperfine structures of the  $^{171}\text{Yb}^+$ , the 369.5 nm laser is delivered through a modulation system consisting of two electro-optical modulators (EOMs) and two acoustic-optical modulators (AOMs). The two EOMs phase modulate the passing laser at 2.11 and 14.7 GHz, respectively; thus, the laser will acquire sidebands in the frequency domain corresponding to the modulation frequencies after passing through them. When the nonmodulated carrier frequency is tuned to resonant with the  $^2S_{1/2} |F=1\rangle \leftrightarrow ^2P_{1/2} |F=0\rangle$  transition, the 1st order sideband from the 2.11 GHz EOM is resonant with the  $^2S_{1/2} |F=1\rangle \leftrightarrow ^2P_{1/2} |F=1\rangle$  transition, and that from the 14.7 GHz (2.11 GHz + 12.6 GHz) EOM is resonant with the transition of  $^2S_{1/2} |F=0\rangle \leftrightarrow ^2P_{1/2} |F=1\rangle$ . The two AOMs are used here as fast optical shutters and frequency shifters, set up in a double-pass (DP) configuration. The switching of all the signal sources used for the EOMs and AOMs is controlled by TTL signals, allowing us to quickly turn on/off each device at the nanosecond level, thus applying a series of different operations accurately in the time sequence.

The laser beam diffracted from the AOM-1 is used to implement the processes of Doppler cooling (14.7 GHz EOM and AOM-1 on simultaneously), optical pumping (2.11 GHz EOM and AOM-1 on simultaneously), and detection (AOM-1 on only). Note that the signal frequency injected into the AOM for Doppler cooling is red-shifted by about 5 MHz (indicating a frequency shift of 10 MHz for laser) from the resonant frequency to achieve the best cooling efficiency. The fluorescence of the ions during detection was collected by an objective lens with a numerical aperture of 0.4, resulting in a state preparation and measurement (SPAM) error of less than  $7 \times 10^{-3}$ .

The other beam diffracted from the AOM-2 is used to engineer the effective gain and damping processes in the targeted qubit system. The polarization of this beam is optimized to be perpendicular to the direction of the magnetic  $B$  field, thus inducing only  $\sigma_+$  and  $\sigma_-$  transitions between the  $^2S_{1/2}$  and  $^2P_{1/2}$  levels. The coupling strengths of the *gain* beam ( $\Omega_g$ ) and the *damping* beam ( $\Omega_d$ ) are determined by the sideband amplitudes generated by the 14.7 GHz and 2.11 GHz EOMs, respectively; therefore, they can be tuned independently by adjusting the signal amplitudes injected into each EOM. The carrier component after passing through the EOMs works as the *repumping* beam. In Appendix B, we would derive the relationships between the values of  $\Gamma_g$ ,  $\Gamma_d$  and the values of  $\Omega_g$ ,  $\Omega_d$ . The external driving signal for synchronization is generated by the frequency mixing and then amplified by a 10 Watt microwave amplifier. The frequency, amplitude, and phase of the driving signal can be precisely controlled by tuning the DDS settings.

## APPENDIX B: EFFECTIVE DISSIPATED QUBIT

In this section, we introduce in theory that how we could obtain an effective dissipated qubit by engineering a multilevel system. Specifically, we utilize the eight-level system of  $^{171}\text{Yb}^+$  to induce controllable damping rate  $\Gamma_d$  and gain rate  $\Gamma_g$  within the target qubit system, as shown in Figs. 2(b) and 10. The Hilbert space of the whole eight-level system can be divided into two subspaces,  $\mathcal{H}_i$  and  $\mathcal{H}_a$ . The target Hilbert space  $\mathcal{H}_i$  includes two levels of  $\{|^2S_{1/2}^{0,0}\rangle \equiv |0\rangle, |^2S_{1/2}^{1,0}\rangle \equiv |1\rangle\}$ , while the remaining six levels  $\{|^2S_{1/2}^{1,\pm 1}\rangle, |^2P_{1/2}^{0,0}\rangle, |^2P_{1/2}^{1,0}\rangle, |^2P_{1/2}^{1,\pm 1}\rangle\}$  make up the auxiliary

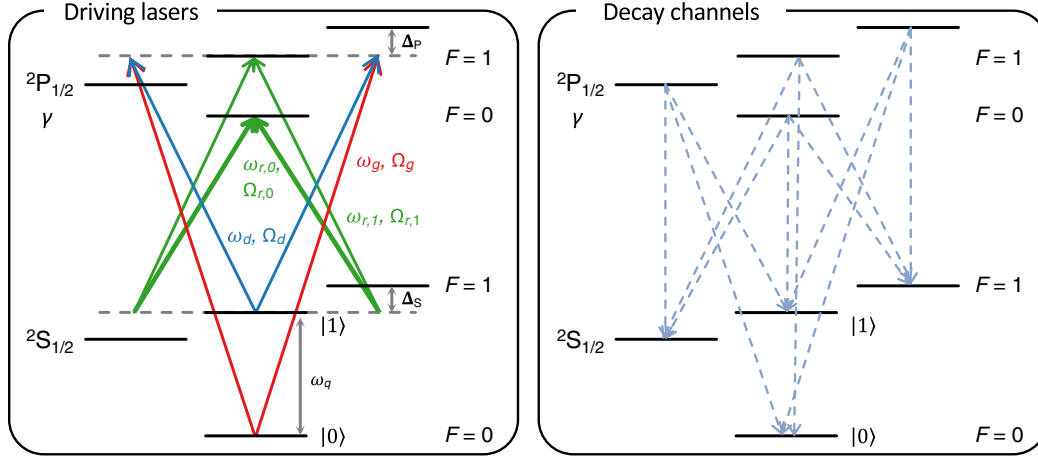


FIG. 10. Energy levels to engineer dissipated qubit system. (Left) All the transitions driven by different laser beams with the optical frequency  $\omega_i$  and coupling strength  $\Omega_i$ . (Right) All possible decay channels from the excited P levels. Note that for each level there are three channels with equal decay probability.

Hilbert space  $\mathcal{H}_a$ . Here, the notation of  $|^{2S+1}L_J^{F,m_F}\rangle$  represents the energy level  $^{2S+1}L_J|F, m_F\rangle$ . As shown in Fig. 10, we experimentally set  $\Omega_d, \Omega_g, \Omega_{r,1} \ll \Omega_{r,0} \sim \gamma$ , where  $\Omega_{d,g,r}$  are the coupling strengths of the applied lasers and  $\gamma$  is the spontaneous emission rate. This setting results in that the ion stays in target Hilbert space for almost all time, and then we could adiabatically eliminate all the auxiliary states and obtain an effective Lindblad master equation for the two-level open system [48].

To derive the effective master equation, we follow the adiabatic elimination method introduced in Ref. [48]. For a general open system, we have the Lindblad master equation,

$$\frac{d\hat{\rho}}{dt} = -i[\hat{H}, \hat{\rho}] + \sum_k \mathcal{D}[\hat{L}_k]\hat{\rho}, \quad (\text{B1})$$

where  $\mathcal{D}[\hat{A}]\hat{\rho} = \hat{A}\hat{\rho}\hat{A}^\dagger - \frac{1}{2}\{\hat{A}^\dagger\hat{A}, \hat{\rho}\}$  is the Lindblad superoperator, and  $\hat{H} = \hat{H}_t + \hat{H}_a + \hat{V}_t + \hat{V}_a$ .  $\hat{H}_t$  ( $\hat{H}_a$ ) is the free Hamiltonian of the target (auxiliary) Hilbert space.  $\hat{V}_t$  ( $\hat{V}_a$ ) are the couplings with target (auxiliary) Hilbert space being the destination levels. Based on the perturbation theory and the adiabatic elimination method, Eq. (B1) can be reduced to an effective master equation of the target Hilbert space as below,

$$\frac{d\hat{\rho}_t}{dt} = -i[\hat{H}_{\text{eff}}, \hat{\rho}_t] + \sum_k \mathcal{D}[\hat{L}_{\text{eff}}^k]\hat{\rho}_t, \quad (\text{B2})$$

where  $\hat{\rho}_t$  represents the density matrix of the targeted system, and the effective Hamiltonian  $\hat{H}_{\text{eff}}$  reads

$$\hat{H}_{\text{eff}} = -\frac{1}{2} \left[ \hat{V}_t(t) \sum_{l,n} (\hat{H}_{\text{NH}}^{(l,n)})^{-1} \hat{V}_a^{(l,n)}(t) + \text{H.c.} \right] + \hat{H}_t. \quad (\text{B3})$$

Moreover, the effective Lindblad operators in Eq. (B2) can be expressed as

$$\hat{L}_{\text{eff}}^k = \hat{L}_k \sum_{l,n} (\hat{H}_{\text{NH}}^{(l,n)})^{-1} \hat{V}_a^{(l,n)}(t). \quad (\text{B4})$$

Here,  $(\hat{H}_{\text{NH}}^{(l,n)})^{-1} = (\hat{H}_{\text{NH}} - E_n - \omega_l)^{-1}$ , and  $\hat{V}_a^{(l,n)}$  is the coupling element for the field  $l$  with the frequency of  $\omega_l$  and the associated initial state is  $|n\rangle$  with energy  $E_n$ . The

non-Hermitian Hamiltonian  $\hat{H}_{\text{NH}}$  in Eqs. (B3) and (B4) reads as below,

$$\hat{H}_{\text{NH}} = \hat{H}_a - \frac{i}{2} \sum_k \hat{L}_k^\dagger \hat{L}_k. \quad (\text{B5})$$

For our situation, the free Hamiltonians of target and auxiliary subspace can be written as

$$\hat{H}_t = \frac{\omega_q}{2} \hat{\sigma}_z, \quad (\text{B6})$$

$$\begin{aligned} \hat{H}_a = & \sum_{m=\pm 1} E_S^{1,m_F} |^2S_{1/2}^{1,m_F}\rangle \langle ^2S_{1/2}^{1,m_F}| \\ & + \sum_{F,m_F} E_P^{F,m_F} |^2P_{1/2}^{F,m_F}\rangle \langle ^2P_{1/2}^{F,m_F}|. \end{aligned} \quad (\text{B7})$$

Here,  $E_L^{F,m_F}$  is the eigenenergy of the energy level  $|^{2S+1}L_J^{F,m_F}\rangle$ , and the qubit energy gap  $\omega_q$  is equal to  $E_S^{1,0} - E_S^{0,0}$ . Meanwhile, the coupling operators induced by the driving lasers (shown in Fig. 10) can be summarized as follows:

$$\begin{aligned} \hat{V}_t = & \frac{1}{2} (\Omega_g e^{i\omega_g t} |0\rangle + \Omega_d e^{i\omega_d t} |1\rangle) \\ & \times (|^2P_{1/2}^{1,-1}\rangle + |^2P_{1/2}^{1,1}\rangle), \end{aligned} \quad (\text{B8})$$

$$\begin{aligned} \hat{V}_a - \hat{V}_t^\dagger = & \frac{\Omega_{r,0} e^{i\omega_{r,0} t}}{2} |^2P_{1/2}^{0,0}\rangle (|^2S_{1/2}^{1,-1}\rangle + |^2S_{1/2}^{1,1}\rangle) \\ & + \frac{\Omega_{r,1} e^{i\omega_{r,1} t}}{2} |^2P_{1/2}^{1,0}\rangle (|^2S_{1/2}^{1,-1}\rangle + |^2S_{1/2}^{1,1}\rangle) \\ & + \text{H.c.} \end{aligned} \quad (\text{B9})$$

The spontaneous emission from the excited P levels can be described as the Lindblad operators as below,

$$\hat{L}^{(F,m_F) \rightarrow (F',m_{F'})} = \sqrt{\frac{\gamma}{3}} |^2S_{1/2}^{F',m_{F'}}\rangle \langle ^2P_{1/2}^{F,m_F}|. \quad (\text{B10})$$

All the possible decay channels are listed in the right subfigure of Fig. 10. The coefficient of  $\sqrt{\gamma/3}$  is because that each P level has three decay channels with equal probability. After

inserting Eqs. (B7) and (B10) into Eq. (B5), we can obtain the following non-Hermitian Hamiltonian  $\hat{H}_{\text{NH}}$ :

$$\hat{H}_{\text{NH}} = \hat{H}_a - \frac{i\gamma}{2} \sum_{F, m_F} |^2P_{1/2}^{F, m_F}\rangle \langle ^2P_{1/2}^{F, m_F}|. \quad (\text{B11})$$

Now we can calculate the effective Hamiltonian of the targeted system  $\hat{H}_{\text{eff}}$  by utilizing the relation of Eq. (B12), and after simplification we find that

$$\hat{H}_{\text{eff}} = \hat{H}_t. \quad (\text{B12})$$

Furthermore, the engineered dissipation within the qubit system can be characterize by the effective Lindblad operators, which are written as

$$\begin{aligned} \hat{L}_{\text{eff}}^{(1, \pm 1) \rightarrow (F, 0)} &= \sqrt{\frac{\gamma}{3}} \frac{\Omega_g e^{-i\omega_g t}}{\pm 2\Delta_P - i\gamma} |F\rangle \langle 0| \\ &+ \sqrt{\frac{\gamma}{3}} \frac{\Omega_d e^{-i\omega_d t}}{\pm 2\Delta_P - i\gamma} |F\rangle \langle 1|. \end{aligned} \quad (\text{B13})$$

Note that, the ion stays at the levels of  $|^2P_{1/2}^{1, \pm 1}\rangle$  would also have 1/3 probability to decay to the levels of  $|^2S_{1/2}^{1, \pm 1}\rangle$ , respectively, and the strong repumping transitions from  $|^2S_{1/2}^{1, \pm 1}\rangle$  to  $|^2P_{1/2}^{1, 0}\rangle$  and  $|^2P_{1/2}^{1, 1}\rangle$  have the coupling strengths of  $\Omega_{r,1} \ll \Omega_{r,0} \sim \gamma$ . Therefore we assume that the repumping process occurs almost instantaneously, and the effective Lindblad operators with the instantaneous repumping can be modified as

$$\begin{aligned} \hat{L}_{\text{eff, repump}}^{(1, \pm 1) \rightarrow (1, 0)} &= \sqrt{\frac{2\gamma}{3}} \frac{\Omega_g e^{-i\omega_g t}}{\pm 2\Delta_P - i\gamma} |1\rangle \langle 0| \\ &+ \sqrt{\frac{2\gamma}{3}} \frac{\Omega_d e^{-i\omega_d t}}{\pm 2\Delta_P - i\gamma} |1\rangle \langle 1|, \end{aligned} \quad (\text{B14})$$

$$\begin{aligned} \hat{L}_{\text{eff, repump}}^{(1, \pm 1) \rightarrow (0, 0)} &= \sqrt{\frac{\gamma}{3}} \frac{\Omega_g e^{-i\omega_g t}}{\pm 2\Delta_P - i\gamma} |0\rangle \langle 0| \\ &+ \sqrt{\frac{\gamma}{3}} \frac{\Omega_d e^{-i\omega_d t}}{\pm 2\Delta_P - i\gamma} |0\rangle \langle 1|. \end{aligned} \quad (\text{B15})$$

Here, the coefficients in Eq. (B14) are modified from  $\sqrt{\gamma/3}$  to  $\sqrt{2\gamma/3}$ , because we assume that the leakage to the levels of  $|^2S_{1/2}^{1, \pm 1}\rangle$  is almost repumped back to the  $|1\rangle$  state under the situation of  $\Omega_{r,0} \gg \Omega_{r,1}$ . Then the effective Lindblad super-operators of the target Hilbert subspace turn out to be

$$\begin{aligned} \mathcal{D}[\hat{L}_{\text{eff, repump}}^{(1, \pm 1) \rightarrow (1, 0)}] \hat{\rho}_t &\approx \frac{2\gamma}{3} \frac{\Omega_g^2}{4\Delta_P^2 + \gamma^2} \mathcal{D}[\hat{\sigma}_+] \hat{\rho}_t \\ &+ \frac{2\gamma}{3} \frac{\Omega_d^2}{4\Delta_P^2 + \gamma^2} \mathcal{D}[|1\rangle \langle 1|] \hat{\rho}_t, \end{aligned} \quad (\text{B16})$$

$$\begin{aligned} \mathcal{D}[\hat{L}_{\text{eff, repump}}^{(1, \pm 1) \rightarrow (0, 0)}] \hat{\rho}_t &\approx \frac{\gamma}{3} \frac{\Omega_g^2}{4\Delta_P^2 + \gamma^2} \mathcal{D}[|0\rangle \langle 0|] \hat{\rho}_t \\ &+ \frac{\gamma}{3} \frac{\Omega_d^2}{4\Delta_P^2 + \gamma^2} \mathcal{D}[\hat{\sigma}_-] \hat{\rho}_t. \end{aligned} \quad (\text{B17})$$

All the high-frequency oscillating terms are ignored, because in our experimental setup, the frequency difference of  $\omega_g - \omega_d$  is much great than the energy scale of the decay and coupling strengths. Combining Eqs. (B16) and (B17), we can finally

obtain the effective dissipation on the qubit system as below,

$$\begin{aligned} \mathcal{L}_0 \hat{\rho}_t &= \sum_{m=\pm 1, F=0, 1} \mathcal{D}[\hat{L}_{\text{eff, repump}}^{(1, m) \rightarrow (F, 0)}] \hat{\rho}_t \\ &= \frac{\Gamma_g}{2} \mathcal{D}[\hat{\sigma}_+] \hat{\rho} + \frac{\Gamma_d}{2} \mathcal{D}[\hat{\sigma}_-] \hat{\rho} + \frac{\Gamma_z}{2} \mathcal{D}[\hat{\sigma}_z] \hat{\rho}, \end{aligned} \quad (\text{B18})$$

where

$$\begin{aligned} \Gamma_g &= \frac{8\gamma}{3} \frac{\Omega_g^2}{4\Delta_P^2 + \gamma^2}, \\ \Gamma_d &= \frac{4\gamma}{3} \frac{\Omega_d^2}{4\Delta_P^2 + \gamma^2}, \\ \Gamma_z &= \frac{\gamma}{3} \frac{2\Omega_d^2 + \Omega_g^2}{4\Delta_P^2 + \gamma^2}. \end{aligned} \quad (\text{B19})$$

Note that, the values of  $\Gamma_g$  and  $\Gamma_d$  can be controlled respectively by adjusting the strengthes of  $\Omega_g$  and  $\Omega_d$ , while  $\Gamma_z$  is determined afterwards, which can not be independently tuned.

### APPENDIX C: CONSTRUCTING $Q$ FUNCTION AND $S$ FUNCTION

Here, we show how to obtain  $Q$  and  $S$  functions in experiments. It is straightforward to measure the above two functions if the sync signal is resonant to the qubit frequency, which means  $\hat{U}_q = \hat{U}_s$ . By applying single-qubit rotations on the desired qubit state  $\hat{\rho}$  and then measuring the state probability on the  $|1\rangle$  state, we can directly calculate the value of  $Q(\theta, \phi)$  based on the relation of

$$\begin{aligned} Q(\theta, \phi) &= \frac{1}{2\pi} \langle \theta, \phi | \hat{\rho} | \theta, \phi \rangle \\ &= \frac{1}{2\pi} \text{Tr}[e^{-i\theta \hat{\sigma}_\phi - \pi/2} \hat{\rho} e^{i\theta \hat{\sigma}_\phi - \pi/2} (|1\rangle \langle 1|)], \end{aligned} \quad (\text{C1})$$

where  $\hat{\sigma}_\phi = \hat{\sigma}_x \cos \phi + \hat{\sigma}_y \sin \phi$ . And then the corresponding  $S$  function can be constructed through the discrete integration of the  $\{Q(\theta_i, \phi_j)\}$  obtained in the experiment. Above methods are applied to obtain the  $Q$  and  $S$  functions in Figs. 4(b)–4(g) and  $Q$  functions in the inset figures of Fig. 6(a).

However, above methods to obtain the  $S$  function is inefficient. Instead, we can just measure the Bloch vector  $\mathbf{m} = \{m_x, m_y, m_z\}$  of the qubit state  $\hat{\rho}$  and then use the relation of,

$$S(\phi) = \frac{1}{8} (m_x \cos \phi + m_y \sin \phi), \quad (\text{C2})$$

to construct the  $S$  function, where  $m_i = \text{Tr}[\sigma_i \rho]$ . In the resonant driving case ( $\hat{U}_q = \hat{U}_s$ ), we can obtain the components of the Bloch vector by applying the analysis pulses in the set that including  $e^{i\Omega_{\text{MW}} \tau_\pi \sigma_y / 4}$ ,  $e^{-i\Omega_{\text{MW}} \tau_\pi \sigma_x / 4}$  and  $I$ , to the qubit and then measure the probability of projecting to the  $|1\rangle$  state. Here  $\Omega_{\text{MW}}$ ,  $\tau_\pi$  are the coupling strength and the duration of the analysis pulse, respectively and satisfy the relation of  $\Omega_{\text{MW}} \tau_\pi = \pi$ . The measurement results of each analysis pulse correspond to the value of  $(m_x + 1)/2$ ,  $(m_y + 1)/2$  and  $(m_z + 1)/2$ , respectively. In the experiments, we set  $\Omega_{\text{MW}}$  and  $\tau_\pi$  to be  $(2\pi) \times 32.0(1)$  kHz and 15.6  $\mu\text{s}$ , respectively. However, when the sync signal is detuned away from the qubit resonant frequency, the above method fails because the synchronized state and the analysis pulses are not in the same rotating frame ( $\hat{U}_q \neq \hat{U}_s$ ). In this case, we use a set

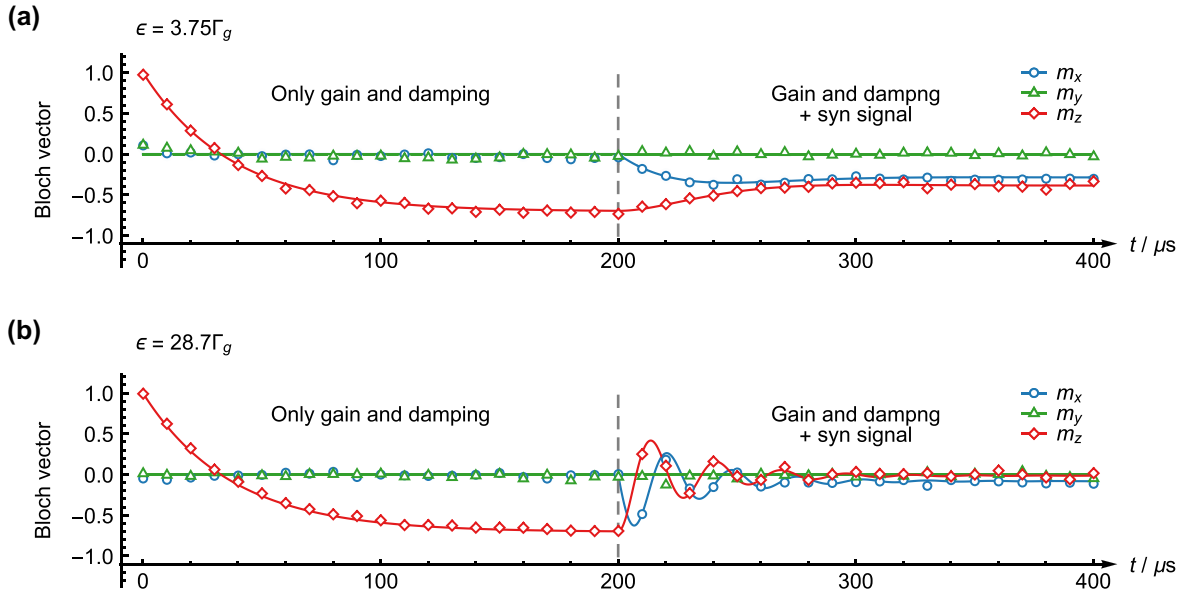


FIG. 11. Time evolution of the Bloch vector under different sync strengths. The results in (a) and (b) correspond to the sync signals with the strengths of  $3.75\Gamma_g$  and  $28.7\Gamma_g$ , respectively. The open markers and the solid lines represent the experiment and simulation results for each Bloch vector component.

of nonorthogonal analysis pulses including  $e^{-i(\Delta\sigma_z + \Omega_{MW}\sigma_x)\tau_\pi/4}$ ,  $e^{-i(\Delta\sigma_z + \Omega_{MW}\sigma_x)\tau_\pi/2}$ ,  $e^{-i(\Delta\sigma_z + \Omega_{MW}\sigma_y)\tau_\pi/4}$ ,  $e^{-i(\Delta\sigma_z + \Omega_{MW}\sigma_y)\tau_\pi/2}$ , and  $I$ . depending on the detuning  $\Delta$ . The Bloch vector can be estimated by using Maximum likelihood estimation on the measurement results. This method is used to obtain the results in Fig. 5.

#### APPENDIX D: QUANTUM SYNCHRONIZATION UNDER DIFFERENT SYNC STRENGTHS

In Fig. 6(c), we show the experimental results about the time evolution of the Bloch vector component  $m_z$  under different sync strengths. Here, we supplement the time evolution for all other components, as shown in Fig. 11.

#### APPENDIX E: CLASSICAL MOTION OF DISSIPATED QUANTUM SYSTEMS

Here, we complement the classical motion analysis of vdP oscillators and damped oscillators. Their behavior can be used to compare with that of the dissipated qubit. Furthermore, by using the evolution equations of the operators, we attempt to analyze the nonlinear dynamics of dissipated spin systems.

##### 1. Quantum oscillators

First let us recall the driven quantum vdP oscillator, whose state evolution is governed by the following Lindblad equation:

$$\frac{d\hat{\rho}}{dt} = -i[v\hat{a}^\dagger\hat{a} + \epsilon(\hat{a} + \hat{a}^\dagger)\cos(\omega t + \varphi), \rho] + \kappa_1\mathcal{D}[\hat{a}^\dagger]\hat{\rho} + \kappa_2\mathcal{D}[\hat{a}^2]\hat{\rho}. \quad (\text{E1})$$

To explore the motion dynamics in the phase space, we consider the evolution of the annihilation operator  $\hat{a}$  in the

Heisenberg picture as follows:

$$\frac{d\hat{a}}{dt} = i[v\hat{a}^\dagger\hat{a} + \epsilon(\hat{a} + \hat{a}^\dagger)\cos(\omega t + \varphi), \hat{a}] + \kappa_1\tilde{\mathcal{D}}[\hat{a}^\dagger]\hat{a} + \kappa_2\tilde{\mathcal{D}}[\hat{a}^2]\hat{a}, \quad (\text{E2})$$

where  $\tilde{\mathcal{D}}[\hat{A}]\hat{B} = \hat{A}^\dagger\hat{B}\hat{A} - (\hat{A}^\dagger\hat{A}\hat{B} + \hat{B}\hat{A}^\dagger\hat{A})/2$ . Then Eq. (E2) can be further simplified to be the following form:

$$\frac{d\langle\hat{a}\rangle}{dt} = -iv\langle\hat{a}\rangle + \frac{\kappa_1}{2}\langle\hat{a}\rangle - \kappa_2\langle\hat{a}^\dagger\hat{a}\hat{a}\rangle - i\epsilon\cos(\omega t + \varphi), \quad (\text{E3})$$

where  $\langle\hat{a}\rangle = \text{Tr}[\hat{a}\hat{\rho}]$ .

For convenience, we focus on the case where  $\langle\hat{a}^\dagger\hat{a}\rangle \gg 1$ , indicating that  $\kappa_1$  is much larger than  $\kappa_2$  (assuming that both of them are nonzero). This allows us to further simplify the above equation to the following form:

$$\frac{d\alpha}{dt} = -iv\alpha + \frac{\kappa_1}{2}\alpha - \kappa_2|\alpha|^2\alpha - i\epsilon\cos(\omega t + \varphi). \quad (\text{E4})$$

Here,  $\alpha = \langle\hat{a}\rangle$  is regarded as the ‘‘classical trajectory’’ of the quantum oscillator in the phase space. By representing  $\alpha = re^{-i\phi}$ , we can derive the evolution equations for the oscillation amplitude  $r$  and phase  $\phi$  as follows:

$$\begin{aligned} \frac{dr}{dt} &= \frac{\kappa_1}{2}r - \kappa_2r^3 - \epsilon\cos(\omega t + \varphi)\sin\phi, \\ \frac{d\phi}{dt} &= \omega\phi + \frac{\epsilon}{r}\cos(\omega t + \varphi)\cos\phi. \end{aligned} \quad (\text{E5})$$

In the absence of the external signal ( $\epsilon = 0$ ), the above equations yields a steady-state solution of,

$$\begin{aligned} r(t \rightarrow \infty) &= r_{LC} = \sqrt{\frac{\kappa_1}{2\kappa_2}}, \\ \phi(t) &= \omega t + \phi_0. \end{aligned} \quad (\text{E6})$$



Here the oscillation amplitude has a finite value of  $r_{LC}$ , while the initial phase for the oscillation phase is fully free. This steady-state solution clearly suggests that the trajectory of the quantum vdP oscillator in the phase space would always fall onto a cycle of nonzero radius  $r_{LC}$ , well known as the “limit cycle.”

When the system evolves from the limit cycle, and a weak external signal is triggered simultaneously, the oscillation phase  $\phi$  would be tuned by this external signal with a strength of  $\epsilon/r_{LC}$  (assuming that the amplitude of the external signal is too weak to perturb the limit cycle). Consequently, the frequency of the quantum vdP oscillator would progressively follow that of the external signal, a phenomenon well-known as synchronization.

Similar analysis can be also applied to another well-known dissipated oscillator model, the quantum damped oscillator described by the following Lindblad equations:

$$\frac{d\hat{\rho}}{dt} = -i[v\hat{a}^\dagger\hat{a} + \epsilon(\hat{a} + \hat{a}^\dagger)\cos(\omega t + \varphi), \rho] + \kappa_1\mathcal{D}[\hat{a}]\hat{\rho}. \quad (E7)$$

By applying similar approach utilized in the quantum vdP oscillator, we can obtain the dynamical equations of the classical trajectory for the quantum damped oscillator,

$$\begin{aligned} \frac{dr}{dt} &= -\frac{\kappa_1}{2}r - \epsilon\cos(\omega t + \varphi)\sin\phi, \\ \frac{d\phi}{dt} &= \omega\phi + \frac{\epsilon}{r}\cos(\omega t + \varphi)\cos\phi. \end{aligned} \quad (E8)$$

It is worth noting that for the evolution equation of the oscillation phase  $\phi$ , both the quantum damped oscillator and the quantum vdP oscillator share the same form. However, for the damped oscillator, the steady state of the oscillation amplitude  $r$  turns out to be

$$r(t \rightarrow \infty) = r_{\text{steady}} = 0 \quad (E9)$$

if the external driving is absent ( $\epsilon = 0$ ). Thus no closed trajectory can be found in the phase space.

When the quantum damped oscillator evolves from the above steady state, and disturbed by the external signal, the

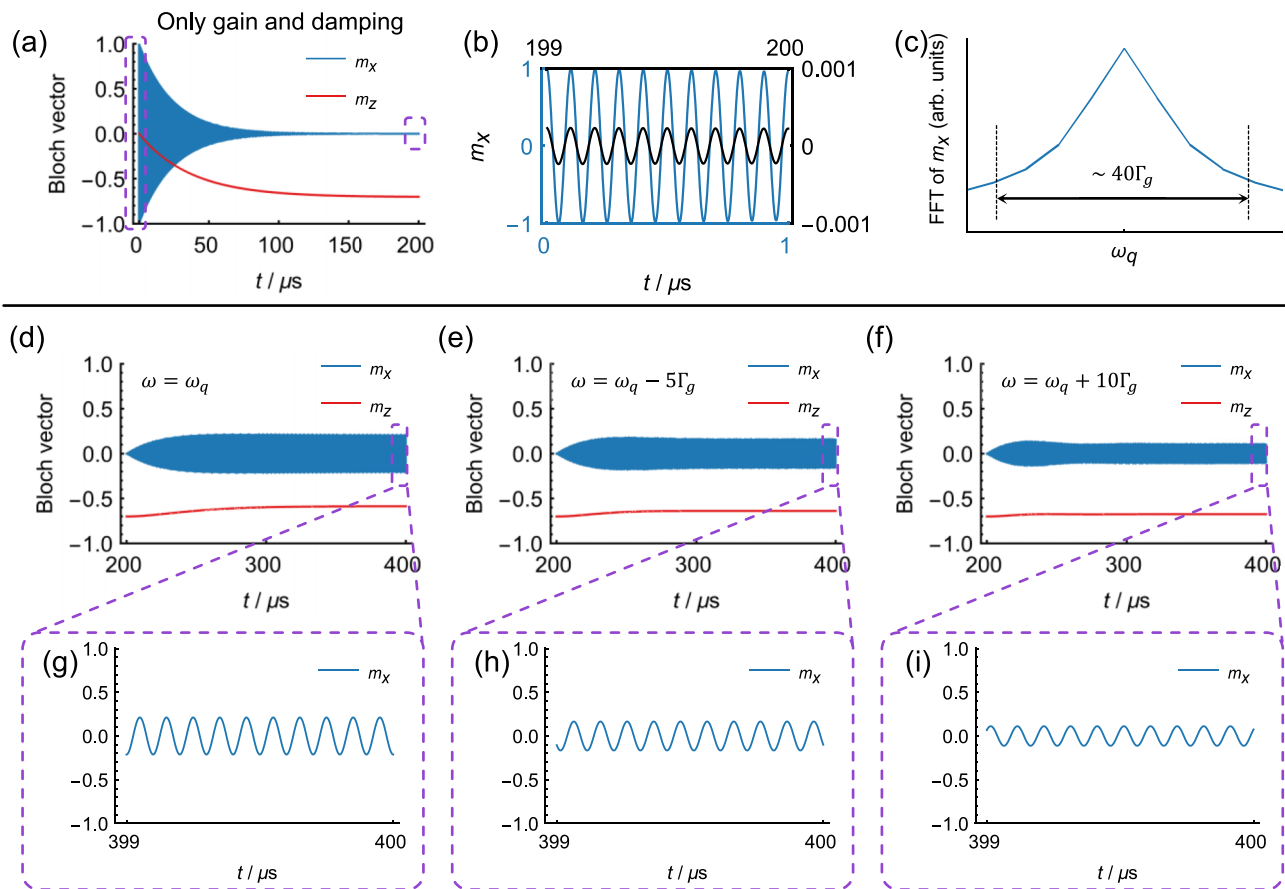


FIG. 12. Dynamics of driven dissipated qubit in Schrodinger picture. (a). Time evolution of the Bloch vector under only dissipations. The initial state is set to  $(|0\rangle + |1\rangle)/\sqrt{2}$ . (b). We zoom in on the time evolution of the Bloch vector shown in (a), specifically focusing on the oscillations in the intervals  $(0.0, 1.0)\ \mu\text{s}$  and  $(199.0, 200.0)\ \mu\text{s}$ . The amplitude of the oscillation decays while the oscillating frequency remains unchanged. (c). We apply the fast Fourier transformation to the simulation data shown in (a), with a sampling interval of  $0.002\ \mu\text{s}$ . The transformed spectral data show a distinct peak at the qubit’s intrinsic frequency  $\omega_q$ . [(d)–(f)]. After the relaxation of the qubit to the limit cycle, we simulate the evolution of the qubit by adding external signals with different parameters. We set the values of the sync frequency to be  $\omega_q$ ,  $\omega_q - 5\Gamma_g$ ,  $\omega_q + 10\Gamma_g$ , corresponding to the results in (d) to (f), respectively. For all cases, we can observe the recovery of the oscillations of the qubit coherence ( $m_x$ ) while the energy of the qubit changes only slightly ( $m_z$ ). [(g)–(i)]. We zoom in on the time evolution from  $399\ \mu\text{s}$  to  $400\ \mu\text{s}$  shown in [(d)–(f)]. The oscillations of the qubit coherence become stable, and the oscillation amplitude decays as the driving frequency of the external signal is tuned away from the qubit frequency.

TABLE I. Capability of synchronization for dissipated qubit.

Dissipation rates	Synchronizable or not	Analogous to quantum oscillator
$\Gamma_g = \Gamma_d$	No	-
$\Gamma_g = 0$ or $\Gamma_d = 0$	No	damped oscillator
All other cases	Yes	vdP oscillator

strength of the phase response to the external signal,  $\epsilon/r_{\text{steady}}$ , becomes infinity. This indicates that the oscillation frequency of the damped oscillator would almost instantaneously reach the external signal frequency. Therefore the dynamics for the quantum damped oscillator should be treated as forced driving instead of synchronization.

Together with the results in Sec. IV, here we summarize all conclusions about synchronizability in Table I.

## 2. Nonlinearity for dynamics of dissipated spin systems

Let us further discuss the “nonlinearity” of the dissipated qubit. For classical oscillator systems, the existence of limit cycles requires systems own certain nonlinearity, such as the presence of the  $x^2x'$  or  $(a^\dagger aa)$  term in the vdP oscillator. Thus we consider exploring whether the dissipated qubit exhibit any “nonlinearity.”

First let us consider the dissipated spin-1 model discussed by Roulet and Bruder [31],

$$\begin{aligned} \frac{d\hat{\rho}}{dt} = & -i[\omega\hat{S}_z, \rho] \\ & + \gamma_g\mathcal{D}[\hat{S}_+\hat{S}_z]\hat{\rho} + \gamma_d\mathcal{D}[\hat{S}_-\hat{S}_z]\hat{\rho}. \end{aligned} \quad (\text{E10})$$

The time evolution of the spin operators in the Heisenberg picture can be expressed as

$$\begin{aligned} \frac{d\langle\hat{S}_x\rangle}{dt} = & \frac{\gamma_g - \gamma_d}{2} \langle\hat{S}_z\hat{S}_x + \hat{S}_x\hat{S}_z\rangle \\ & - \frac{\gamma_g + \gamma_d}{2} \langle\hat{S}_x\rangle - \omega \langle\hat{S}_y\rangle, \\ \frac{d\langle\hat{S}_y\rangle}{dt} = & \frac{\gamma_g - \gamma_d}{2} \langle\hat{S}_z\hat{S}_y + \hat{S}_y\hat{S}_z\rangle \\ & - \frac{\gamma_g + \gamma_d}{2} \langle\hat{S}_y\rangle + \omega \langle\hat{S}_x\rangle, \\ \frac{d\langle\hat{S}_z\rangle}{dt} = & \frac{\gamma_g - \gamma_d}{2} \langle\hat{S}_z\hat{S}_z\rangle - \frac{\gamma_g + \gamma_d}{2} \langle\hat{S}_z\rangle. \end{aligned} \quad (\text{E11})$$

Clearly the terms of  $\langle\hat{S}_z\hat{S}_x + \hat{S}_x\hat{S}_z\rangle$ ,  $\langle\hat{S}_z\hat{S}_y + \hat{S}_y\hat{S}_z\rangle$  and  $\langle\hat{S}_z\hat{S}_z\rangle$  indicate the nonlinear dynamics of the system evolution. This nonlinearity allows the dissipated spin-1 system to own a valid limit cycle. It is also worth noting that when  $\gamma_g = \gamma_d$ , all coefficients of the nonlinear terms become zero. This is consistent with the results given in Ref. [31], that this kind of spin-1 system cannot be synchronized. This further supports the notion that nonlinearity plays a crucial role in the existence of limit cycles even for spin systems.

For the dissipated qubit, we have already shown the evolution of the Pauli operators in Eq. (17). In fact, they are

simplified from the following equations:

$$\begin{aligned} \frac{d\langle\hat{\sigma}_x\rangle}{dt} = & \frac{\Gamma_g - \Gamma_d}{8} \langle\hat{\sigma}_z\hat{\sigma}_x + \hat{\sigma}_x\hat{\sigma}_z\rangle \\ & - \frac{\Gamma_t}{4} \langle\hat{\sigma}_x\rangle - \omega \langle\hat{\sigma}_y\rangle, \\ \frac{d\langle\hat{\sigma}_y\rangle}{dt} = & \frac{\Gamma_g - \Gamma_d}{8} \langle\hat{\sigma}_z\hat{\sigma}_y + \hat{\sigma}_y\hat{\sigma}_z\rangle \\ & - \frac{\Gamma_t}{4} \langle\hat{\sigma}_y\rangle + \omega \langle\hat{\sigma}_x\rangle, \\ \frac{d\langle\hat{\sigma}_z\rangle}{dt} = & \frac{\Gamma_g - \Gamma_d}{4} \langle\hat{\sigma}_z\hat{\sigma}_z\rangle - \frac{\Gamma_g + \Gamma_d}{4} \langle\hat{\sigma}_z\rangle, \end{aligned} \quad (\text{E12})$$

which have similar forms as the spin-1 system. We can also notice the nonlinear terms of  $\langle\hat{\sigma}_z\hat{\sigma}_x + \hat{\sigma}_x\hat{\sigma}_z\rangle$ ,  $\langle\hat{\sigma}_z\hat{\sigma}_y + \hat{\sigma}_y\hat{\sigma}_z\rangle$  and  $\langle\hat{\sigma}_z\hat{\sigma}_z\rangle$ . Unfortunately, the first two terms of  $\langle\hat{\sigma}_z\hat{\sigma}_x + \hat{\sigma}_x\hat{\sigma}_z\rangle$  and  $\langle\hat{\sigma}_z\hat{\sigma}_y + \hat{\sigma}_y\hat{\sigma}_z\rangle$  turn out to be 0 due to the anti-commutation relations of the Pauli operators.

However, it is worth noting that the term of  $\langle\hat{\sigma}_z\hat{\sigma}_z\rangle$  does not vanish but leave a constant here due to the relation  $\hat{\sigma}_z\hat{\sigma}_z = \hat{I}$  where  $\hat{I}$  is the identity matrix. This constant term makes the above evolution equations cannot be expressed as a simple linear transformation, playing as the role of “nonlinearity” in the system evolution. Therefore we regard it as the reason that why the dissipated qubit could own a valid limit cycle.

If we take  $\Gamma_g = \Gamma_d$ , the constant term vanishes. This aligns with our previous analysis, in which this particular dissipated qubit is unsynchronizable. Furthermore, when either  $\Gamma_d$  or  $\Gamma_g$  becomes zero, the equation for  $\langle\hat{\sigma}_z\rangle$  can be revised as follows:

$$\frac{d}{dt}(1 - \langle\hat{\sigma}_z\rangle) = -\frac{\Gamma_g}{8}(1 - \langle\hat{\sigma}_z\rangle) \quad \text{for } \Gamma_d = 0, \quad (\text{E13})$$

or

$$\frac{d}{dt}(1 + \langle\hat{\sigma}_z\rangle) = -\frac{\Gamma_d}{8}(1 + \langle\hat{\sigma}_z\rangle) \quad \text{for } \Gamma_g = 0, \quad (\text{E14})$$

In both of these cases, the operator evolutions can be rewritten into a linear form, indicating the absence of nonlinearity for the system’s dynamics. Consequently, in these scenarios, the qubit cannot be synchronized as well, according to our previous discussions. These findings emphasize the crucial role of nonlinearity in determining the synchronizability of dissipated spin systems.

## APPENDIX F: NUMERICAL SIMULATION OF DRIVEN DISSIPATED QUBIT IN THE SCHRÖDINGER PICTURE

In Sec. II, we have shown how to characterize the synchronization in a rotating frame, where the actual rotation of qubit is canceled by rotating the measurement axis simultaneously. Here, as a supplementary, we numerically simulate the dynamics of the driven dissipated qubit in the Schrödinger picture by directly solving the following master equation:

$$\begin{aligned} \frac{d\hat{\rho}}{dt} = & -i\left[\frac{\omega_q}{2}\hat{\sigma}_z + \epsilon\hat{\sigma}_x \cos(\omega t + \varphi), \hat{\rho}\right] \\ & + \frac{\Gamma_g}{2}\mathcal{D}[\hat{\sigma}_+]\hat{\rho} + \frac{\Gamma_d}{2}\mathcal{D}[\hat{\sigma}_-]\hat{\rho} + \frac{\Gamma_z}{2}\mathcal{D}[\hat{\sigma}_z]\hat{\rho}. \end{aligned} \quad (\text{F1})$$

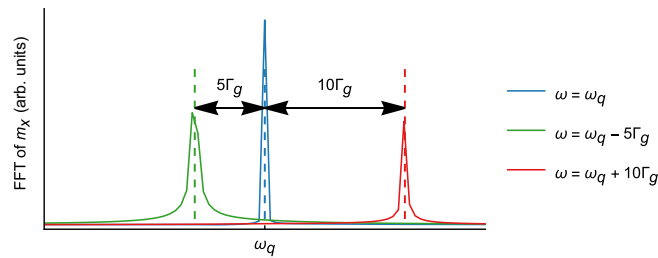


FIG. 13. Spectral analysis on the synchronized qubit. Based on the simulation data shown in Fig. 12(d)–12(f), we apply the fast Fourier transformation to the data in the interval (300, 2000)  $\mu\text{s}$  (400 to 2000  $\mu\text{s}$  not shown in Fig. 12), with a sampling interval of 0.002  $\mu\text{s}$ . It is clear that the qubit oscillates at the frequency of the external signal rather than its intrinsic frequency.

In our numerical simulation, we set most of the parameters in Eq. (F1) to be consistent with the experimental settings,

$$\begin{aligned} \epsilon &= 2\pi \times 2.37 \text{ kHz}, \\ \varphi &= \pi/2, \\ \Gamma_g &= 2\pi \times 1.27 \text{ kHz}, \\ \Gamma_d &= 2\pi \times 7.33 \text{ kHz}, \\ \Gamma_z &= 2\pi \times 4.42 \text{ kHz}, \end{aligned} \quad (\text{F2})$$

and sync frequency  $\omega$  is a tunable parameter in the simulation. Meanwhile, to reduce the time overhead of the numerical simulation, without the loss of the generality, we assume the value of  $\omega_q$  to be  $2\pi \times 10$  MHz instead of the actual value of  $2\pi \times 12.6$  GHz in the experiment. But the rotating wave approximation remains valid if we choose  $\omega$  to make  $|\omega_q - \omega|$  on the order of  $\Gamma_g$ ; therefore, we can still use Eq. (1) to describe the dynamics of the qubit in the rotating frame.

Following the sequence, we utilized in the experimental demonstration, we also divide the evolution into two stages in the numerical simulation, and the results are summarized in

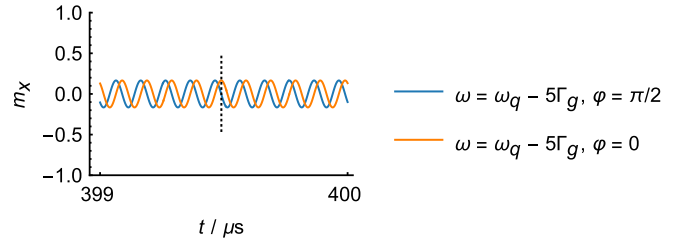


FIG. 14. Phase shift in qubit oscillations. Under the external frequency of  $\omega_q - 5\Gamma_g$ , we shift the initial phase of the external signal from  $\varphi = 0$  to  $\varphi = \pi/2$ , and a  $\pi/2$  phase shift is observed in the qubit oscillations as well.

Fig. 12. During the first stage (lasting 200  $\mu\text{s}$ ), the qubit only suffers from the dissipations while the external sync signal is absent, allowing the qubit to relax to the limit cycle, as shown in Figs. 12(a) and 12(b). Here, in order to illustrate the oscillation of the qubit coherence  $m_x$ , the initial state of the qubit is set to  $(|0\rangle + |1\rangle)/\sqrt{2}$  instead of the  $|1\rangle$  used in the experiments. The results from fast Fourier transformation of data in Fig. 12(a) reveals a single peak at the frequency of  $\omega_q$ .

From 200  $\mu\text{s}$  an external driving signal is added. Here, we choose three values of the driving frequency,  $\omega = \omega_q$ ,  $\omega_q - 5\Gamma_g$ ,  $\omega_q + 10\Gamma_g$ , to observe the response of the qubit dynamics. The results are summarized in Figs. 12(d)–12(i). From all the cases, we can clearly observe the recovery of the oscillation of the qubit coherence. To quantify the frequency of the recovered oscillations, we perform the fast Fourier transform on the steady oscillation data from 300 to 2000  $\mu\text{s}$  [the data points from 400 to 2000  $\mu\text{s}$  are not shown in Figs. 12(d)–12(f)]. The corresponding spectral results are shown in Fig. 13. It is obvious to see three peaks at the frequencies of  $\omega_q$ ,  $\omega_q - 5\Gamma_g$  and  $\omega_q + 10\Gamma_g$ , which are well consistent with the corresponding frequencies of the external signals. Moreover, if we alter the starting phase of the external signal, this phase shift can also be seen in the oscillation of the qubit coherence, as in Fig. 14.

- [1] A. Bell, “The horologium oscillatorium of christian huygens”, *Nature (London)* **148**, 245 (1941).
- [2] L. M. Pecora and T. L. Carroll, Synchronization in Chaotic Systems, *Phys. Rev. Lett.* **64**, 821 (1990).
- [3] N. F. Rulkov, Images of synchronized chaos: Experiments with circuits, *Chaos* **6**, 262 (1996).
- [4] C. Schäfer, M. G. Rosenblum, J. Kurths, and H.-H. Abel, Heart-beat synchronized with ventilation, *Nature (London)* **392**, 239 (1998).
- [5] R. E. Goldstein, M. Polin, and I. Tuval, Noise and Synchronization in Pairs of Beating Eukaryotic Flagella, *Phys. Rev. Lett.* **103**, 168103 (2009).
- [6] J. Fell and N. Axmacher, The role of phase synchronization in memory processes, *Nat. Rev. Neurosci.* **12**, 105 (2011).
- [7] M. H. Matheny, M. Grau, L. G. Villanueva, R. B. Karabalin, M. C. Cross, and M. L. Roukes, Phase Synchronization of Two Anharmonic Nanomechanical Oscillators, *Phys. Rev. Lett.* **112**, 014101 (2014).
- [8] A. Pikovsky, M. Rosenblum, and J. Kurths, *Synchronization: A Universal Concept in Nonlinear Sciences* (Cambridge University Press, Cambridge, UK, 2001).
- [9] A. A. Andronov, A. A. Vitt, and S. E. Khaikin, *Theory of Oscillators*, Adiwes International Series in Physics (Elsevier, Amsterdam, 2013).
- [10] T. D. Ladd, F. Jelezko, R. Laflamme, Y. Nakamura, C. Monroe, and J. L. O’Brien, Quantum computers, *Nature (London)* **464**, 45 (2010).
- [11] J. Preskill, Quantum computing in the NISQ era and beyond, *Quantum* **2**, 79 (2018).
- [12] Y. Alexeev, D. Bacon, K. R. Brown, R. Calderbank, L. D. Carr, F. T. Chong, B. DeMarco, D. Englund, E. Farhi, B. Fefferman, A. V. Gorshkov, A. Houck, J. Kim, S. Kimmel, M. Lange, S. Lloyd, M. D. Lukin, D. Maslov, P. Maunz, C. Monroe *et al.*, Quantum computer systems for scientific discovery, *PRX Quantum* **2**, 017001 (2021).

- [13] O. V. Zhirov and D. L. Shepelyansky, Quantum synchronization, *Eur. Phys. J. D* **38**, 375 (2006).
- [14] I. Goychuk, J. Casado-Pascual, M. Morillo, J. Lehmann, and P. Hänggi, Quantum Stochastic Synchronization, *Phys. Rev. Lett.* **97**, 210601 (2006).
- [15] O. V. Zhirov and D. L. Shepelyansky, Synchronization and Bistability of a Qubit Coupled to a Driven Dissipative Oscillator, *Phys. Rev. Lett.* **100**, 014101 (2008).
- [16] M. A. Lohe, Quantum synchronization over quantum networks, *J. Phys. A: Math. Theor.* **43**, 465301 (2010).
- [17] A. Mari, A. Farace, N. Didier, V. Giovannetti, and R. Fazio, Measures of Quantum Synchronization in Continuous Variable Systems, *Phys. Rev. Lett.* **111**, 103605 (2013).
- [18] T. E. Lee and H. R. Sadeghpour, Quantum Synchronization of Quantum van der Pol Oscillators with Trapped Ions, *Phys. Rev. Lett.* **111**, 234101 (2013).
- [19] S. Walter, A. Nunnenkamp, and C. Bruder, Quantum Synchronization of a Driven Self-Sustained Oscillator, *Phys. Rev. Lett.* **112**, 094102 (2014).
- [20] M. Xu, D. A. Tieri, E. C. Fine, J. K. Thompson, and M. J. Holland, Synchronization of Two Ensembles of Atoms, *Phys. Rev. Lett.* **113**, 154101 (2014).
- [21] H. Eneriz, D. Rossatto, F. A. Cárdenas-López, E. Solano, and M. Sanz, Degree of quantumness in quantum synchronization, *Sci. Rep.* **9**, 19933 (2019).
- [22] T. E. Lee, C.-K. Chan, and S. Wang, Entanglement tongue and quantum synchronization of disordered oscillators, *Phys. Rev. E* **89**, 022913 (2014).
- [23] S. Walter, A. Nunnenkamp, and C. Bruder, Quantum synchronization of two Van der Pol oscillators, *Ann. Phys.* **527**, 131 (2015).
- [24] N. Lörch, S. E. Nigg, A. Nunnenkamp, R. P. Tiwari, and C. Bruder, Quantum Synchronization Blockade: Energy Quantization Hinders Synchronization of Identical Oscillators, *Phys. Rev. Lett.* **118**, 243602 (2017).
- [25] S. Sonar, M. Hajdušek, M. Mukherjee, R. Fazio, V. Vedral, S. Vinjanampathy, and L.-C. Kwek, Squeezing Enhances Quantum Synchronization, *Phys. Rev. Lett.* **120**, 163601 (2018).
- [26] S. Dutta and N. R. Cooper, Critical Response of a Quantum van der Pol Oscillator, *Phys. Rev. Lett.* **123**, 250401 (2019).
- [27] A. Chia, L. C. Kwek, and C. Noh, Relaxation oscillations and frequency entrainment in quantum mechanics, *Phys. Rev. E* **102**, 042213 (2020).
- [28] W.-K. Mok, L.-C. Kwek, and H. Heimonen, Synchronization boost with single-photon dissipation in the deep quantum regime, *Phys. Rev. Res.* **2**, 033422 (2020).
- [29] L. Ben Arosh, M. C. Cross, and R. Lifshitz, Quantum limit cycles and the Rayleigh and van der Pol oscillators, *Phys. Rev. Res.* **3**, 013130 (2021).
- [30] B. Van der Pol, LXXXVIII. On “relaxation-oscillations”, *London, Edinburgh, Dublin Philos. Mag. J. Sci.* **2**, 978 (1926).
- [31] A. Roulet and C. Bruder, Synchronizing the Smallest Possible System, *Phys. Rev. Lett.* **121**, 053601 (2018).
- [32] A. Roulet and C. Bruder, Quantum Synchronization and Entanglement Generation, *Phys. Rev. Lett.* **121**, 063601 (2018).
- [33] M. Koppenhöfer and A. Roulet, Optimal synchronization deep in the quantum regime: Resource and fundamental limit, *Phys. Rev. A* **99**, 043804 (2019).
- [34] A. W. Laskar, P. Adhikary, S. Mondal, P. Katiyar, S. Vinjanampathy, and S. Ghosh, Observation of Quantum Phase Synchronization in Spin-1 Atoms, *Phys. Rev. Lett.* **125**, 013601 (2020).
- [35] M. Koppenhöfer, C. Bruder, and A. Roulet, Quantum synchronization on the IBM Q system, *Phys. Rev. Res.* **2**, 023026 (2020).
- [36] R. Gilmore, C. M. Bowden, and L. M. Narducci, Classical-quantum correspondence for multilevel systems, *Phys. Rev. A* **12**, 1019 (1975).
- [37] L.-C. Kwek, No synchronization for qubits, *Physics* **11**, 75 (2018).
- [38] A. Parra-López and J. Bergli, Synchronization in two-level quantum systems, *Phys. Rev. A* **101**, 062104 (2020).
- [39] G. L. Giorgi, F. Galve, and R. Zambrini, Probing the spectral density of a dissipative qubit via quantum synchronization, *Phys. Rev. A* **94**, 052121 (2016).
- [40] B. Buča, C. Booker, and D. Jaksch, Algebraic theory of quantum synchronization and limit cycles under dissipation, *SciPost Phys.* **12**, 097 (2022).
- [41] P. T. H. Fisk, M. J. Sellars, M. A. Lawn, and C. Coles, Accurate measurement of the 12.6 GHz “Clock” transition in trapped  $^{171}\text{Yb}^+$  ions, *IEEE Trans. Ultrason. Ferroelectr. Freq. Control* **44**, 344 (1997).
- [42] S. Olmschenk, K. C. Younge, D. L. Moehring, D. N. Matsukevich, P. Maunz, and C. Monroe, Manipulation and detection of a trapped  $\text{Yb}^+$  hyperfine qubit, *Phys. Rev. A* **76**, 052314 (2007).
- [43] J. Li, A. K. Harter, J. Liu, L. de Melo, Y. N. Joglekar, and L. Luo, Observation of parity-time symmetry breaking transitions in a dissipative Floquet system of ultracold atoms, *Nat. Commun.* **10**, 855 (2019).
- [44] L. Ding, K. Shi, Q. Zhang, D. Shen, X. Zhang, and W. Zhang, Experimental Determination of  $\mathcal{PT}$ -Symmetric Exceptional Points in a Single Trapped Ion, *Phys. Rev. Lett.* **126**, 083604 (2021).
- [45] M. Zhong, M. P. Hedges, R. L. Ahlefeldt, J. G. Bartholomew, S. E. Beavan, S. M. Wittig, J. J. Longdell, and M. J. Sellars, Optically addressable nuclear spins in a solid with a six-hour coherence time, *Nature (London)* **517**, 177 (2015).
- [46] F. Verstraete, M. M. Wolf, and J. Ignacio Cirac, Quantum computation and quantum-state engineering driven by dissipation, *Nat. Phys.* **5**, 633 (2009).
- [47] P. M. Harrington, E. J. Mueller, and K. W. Murch, Engineered dissipation for quantum information science, *Nat. Rev. Phys.* **4**, 660 (2022).
- [48] F. Reiter and A. S. Sørensen, Effective operator formalism for open quantum systems, *Phys. Rev. A* **85**, 032111 (2012).